Congress of the United States

Washington, DC 20515

June 25, 2020

The Honorable Wilbur L. Ross, Jr.
Secretary, U.S. Department of Commerce
1401 Constitution Avenue, N.W.
Washington, D.C. 20230

Secretary Ross,

We write in strong support of the Chumash Heritage National Marine Sanctuary nomination, and we request that you grant a five-year extension for this proposal. Since the National Oceanic and Atmospheric Administration (NOAA) approved this marine sanctuary proposal in 2015, new data, including recent NOAA studies, have only strengthened the case for this sanctuary to be designated.

NOAA released a study in December 2019 showing that California's coastal waters are acidifying at twice the rate of the global average. These high acidity levels are exacerbated by the alarming loss of more than 90% of coastal marine kelp forests, which can absorb carbon dioxide at twice the rate of land-based forests. Additionally, kelp forests provide critical habitat and food sources for a range of species.

Ocean acidification is a serious threat to both marine ecosystems and coastal economies. A NOAA study released this January showed for the first time that *current* ocean acidification levels can damage young Dungeness crabs' shells and sensory organs, threatening the long-term viability of a fishery valued at $220 million annually.

In addition to environmental issues, this proposed marine sanctuary would protect important parts of U.S. history. In 2016, NOAA and the Coast Guard confirmed the archaeological remains off of Point Conception in this proposed area were that of the *USS McCulloch*, which saw action in both the Spanish American War and World War I. Similarly important cultural artifacts from the settlements of the indigenous Chumash Nation that date back nearly 9,000 years have also been identified in the coastal region surrounding the proposal.

Designating the Chumash Heritage National Marine Sanctuary remains relevant and responsive to the national significance criteria and management considerations. The case is further strengthened by new data and discoveries since its successful nomination five years ago. We urge the Office of Marine Sanctuaries to extend this nomination for an additional five years and to move forward with the designation process to protect this critical marine habitat as soon as possible.

Sincerely,

Dianne Feinstein	Kamala Harris	Salud Carbajal
United States Senator	United States Senator	Member of Congress

Enclosures: December 2019 Feinstein to Ross Letter
NOAA Decadal Variability December 2019 Study
NOAA Dungeness Crab Ocean Acidification January 2020 Study
NOAA Office of Marine Sanctuaries McColluch Factsheet

CALIFORNIA

COMMITTEE ON THE JUDICIARY - RANKING MEMBER
SELECT COMMITTEE ON INTELLIGENCE
COMMITTEE ON APPROPRIATIONS
COMMITTEE ON RULES AND ADMINISTRATION

United States Senate

December 23, 2019

The Honorable Wilbur L. Ross, Jr.
Secretary, U.S. Department of Commerce
1401 Constitution Avenue, N.W.
Washington, D.C. 20230

Dear Secretary Ross,

I am deeply concerned by the National Oceanic and Atmospheric Administration's (NOAA) recent study on ocean acidification impacts on the California coastline, and I urge you to take immediate action to combat rising carbon levels in our oceans, including by accelerating the designation of the proposed "Chumash Heritage National Marine Sanctuary."

California's waters are rising in acidity at twice the global average, threatening marine life and contributing to a growing number of costly fishery disasters. In addition creating 600 new jobs, designating the proposed "Chumash Heritage National Marine Sanctuary" would protect sacred sites of the Chumash people, major animal migratory routes, and kelp habitat. California has lost nearly 90% of its kelp forests, which can absorb carbon at twice the rate of land-based forests. The designation of this area would provide an invaluable opportunity to replenish kelp in an area acutely affected by ocean acidification, and I urge NOAA to act as soon as possible.

Although NOAA approved this marine sanctuary proposal in 2015, the agency has yet to move forward with the designation process. NOAA's Office of National Marine Sanctuaries' (NMS) March 2019 coordination report (attached) stated "there is not active evaluation within NOAA at this time to consider moving this site forward for designation", despite the report identifying that the proposed area "contains an internationally significant ecological transition zone, supporting high biological diversity and densities of numerous important species." I respectfully request that you provide a response detailing why NMS is not actively evaluating this important proposal.

I urge you to move forward with and finalize the designation of the proposed "Chumash Heritage National Marine Sanctuary" as soon as possible. Please do not hesitate to reach out to me with any questions, or have your staff contact Alexis Segal at alexis_segal@feinstein.senate.gov in my office.

Sincerely,

Dianne Feinstein
United States Senator

DF: as\kr
Enclosures

WASHINGTON, DC 20510-0504
http://feinstein.senate.gov

nature geoscience

ARTICLES

https://doi.org/10.1038/s41561-019-0499-z

Decadal variability in twentieth-century ocean acidification in the California Current Ecosystem

Emily B. Osborne[1,2*], Robert C. Thunell[3,6], Nicolas Gruber[4], Richard A. Feely[5] and Claudia R. Benitez-Nelson[3]

Oceanic uptake of CO_2 can mitigate climate change, but also results in global ocean acidification. Ocean acidification-related changes to the marine carbonate system can disturb ecosystems and hinder calcification by some organisms. Here, we use the calcification response of planktonic foraminifera as a tool to reconstruct the progression of ocean acidification in the California Current Ecosystem through the twentieth century. Measurements of nearly 2,000 fossil foraminifera shell weights and areas preserved in a marine sediment core showed a 20% reduction in calcification by a surface-dwelling foraminifera species. Using modern calibrations, this response translates to an estimated 35% reduction in carbonate ion concentration, a biologically important chemical component of the carbonate system. Assuming other aspects of the carbonate system, this represents a 0.21 decline in pH, exceeding the estimated global average decline by more than a factor of two. Our proxy record also shows considerable variability that is significantly correlated with Pacific Decadal Oscillation and decadal-scale changes in upwelling strength, a relationship that until now has been obscured by the relatively short observational record. This modulation suggests that climatic variations will play an important role in amplifying or alleviating the anthropogenic signal and progression of ocean acidification in this region.

Since the beginning the industrial era, atmospheric CO_2 levels have risen from 280 ppm to more than 400 ppm; an unprecedented concentration over the past 800,000 years[1]. The oceans have absorbed approximately 27% of this anthropogenic CO_2, which has caused an estimated 0.1 reduction in global mean surface ocean pH: the phenomenon known as ocean acidification[2–6]. Field studies of some of the ocean's major calcium carbonate producing organisms often indicate a negative calcification response, declining $[CO_3^{2-}]$ (for example, refs. [7–13]), although in some instances calcification remains unaffected or is even enhanced (for example, see refs. [14,15]).

Research suggests that ocean acidification is becoming particularly acute in coastal upwelling regions, such as the California Current Ecosystem (CCE), due to their low buffering capacity and the natural upwelling processes that bring CO_2-rich intermediate waters to the ocean surface (for example, ref. [3,16–21]). Models indicate a considerable decline in $[CO_3^{2-}]$ in the CCE and a shoaling of the saturation horizons for each of the $CaCO_3$ mineral polymorphs (calcite Ω_{cal} and aragonite Ω_{arg}) since the onset of the industrial period, reducing the volume of the surface ocean favourable for calcification[20–22]. Modern sampling has identified malformed and dissolved aragonite-secreting pteropods during periods of strong upwelling, when the saturation horizon comes very close to (or even intersects with) the sea surface[7,16,23].

Initial surveys of the global ocean marine carbonate system only began in the late 1970s, well after anthropogenic carbon began altering the marine carbonate system[24]. Within the CCE specifically, consistent in situ observations of carbonate system variables are limited to the last decade (from the California Cooperative Oceanic Fisheries Investigations (CalCOFI), 2009 to present). While these observational records are critically important to our understanding of ocean chemistry, they do not provide a sufficiently long historical record of this phenomenon. The lack of long-term ocean acidification records limits our ability to place recent observations into the context of past change, and hinders an assessment of the impacts of natural decadal climate oscillations on the marine carbonate system. Model simulations can close the knowledge gap, but without constraints from in situ and/or proxy measurements, their validity remains unknown—especially with regard to their skill in capturing variability. Here, we provide a century-long, nearly annually resolved ocean acidification proxy record for the central region of the CCE and investigate the twentieth-century trends and decadal-scale processes at play.

Carbonate chemistry and calcification

A number of studies have demonstrated that the carbonate chemistry of seawater strongly influences the calcification of planktonic foraminifera, leaving a distinct imprint on the thickness of their shells. This has permitted researchers to use shell weight as a proxy for past surface ocean $[CO_3^{2-}]$. However, shell weight also inherently reflects shell size, which is chiefly controlled by the ambient temperature, and perhaps other variables[25–27] see Methods for extended discussion). Here, we use a relatively new shell weight technique[28] that effectively size-normalizes individual shell weights (Methods), called area normalized shell weight (ANSW), which can be used to quantitatively assess shell thickness and, by extension, $[CO_3^{2-}]$. We apply this technique to the ubiquitously occurring surface-mixed-layer species *Globigerina bulloides* to reconstruct ambient-$[CO_3^{2-}]$ over the past 100 years, building on a proof of concept for this species and method by Osborne et al.[29] (Methods). Previous research

[1]Ocean Acidification Program, National Oceanic and Atmospheric Administration, Silver Spring, MD, USA. [2]Cooperative Program for the Advancement of Earth System Science, University Corporation for Atmospheric Research, Boulder, CO, USA. [3]School of the Earth, Ocean and Environment, University of South Carolina, Columbia, SC, USA. [4]Environmental Physics, Institute of Biogeochemistry and Pollutant Dynamics, ETH Zürich, Zurich, Switzerland. [5]Pacific Marine Environmental Laboratory, National Oceanic and Atmospheric Administration, Seattle, WA, USA. [6]Deceased: Robert C. Thunell. *e-mail: emily.osborne@noaa.gov

on *G. bulloides* has suggested that the calcification and growth of this species might also be influenced by ambient temperature, nutrient concentration or 'optimal growth conditions'[30–32]. The study by Osborne et al.[29] examined sediment trap collections and a sediment core record of *G. bulloides* shell weight, area and diameter data to closely evaluate these relationships and provided robust evidence that ANSW is directly controlled by ambient [CO_3^{2-}], rather than by temperature or nutrient concentration ($R^2=0.80$ (where R is the coefficient of multiple correlation), standard error of the estimate $=\pm 16\,\mu mol\,kg^{-1}$) (see Methods for discussion and Extended Data Fig. 1).

Here, the ANSW of nearly 2,000 individual *G. bulloides* shells were measured using 58 sediment samples from a 0.48-m-long box core collected in an anoxic region of the Santa Barbara Basin (SBB; 34° 14' N, 120° 02' W; 580 m water depth: Extended Data Fig. 2). A radioisotope-based age model was developed for this 100 year laminated and unbioturbated sediment core (1898–2006 ± 6 yr) (see Methods and ref. [29]). Downcore ANSW and shell diameter measurements indicate that, on average, *G. bulloides* produced 20% thinner and 7% larger shells, respectively, by the close of the twentieth century relative to those from 1900 (Extended Data Figs. 3 and 4). To assess whether *G. bulloides* shell thickness (and by extension [CO_3^{2-}]) has declined significantly over the core record, we examine decadal population averages of ANSW (Fig. 1). These averages indicate that shell thicknesses from the 1990–2000 populations are significantly thinner than the 1900–1910 populations (95% confidence). The decline in ANSW is further apparent in scanning electron micrographs of the shell wall thicknesses from the top and bottom of the sediment core (Fig. 1). There is an apparent increase in the rate of change that occurs roughly between the first half and the second half of the core. This change in slope seems to be associated with a greater frequency of low [CO_3^{2-}] events occurring in the more recent portion of the record, thereby reducing the overall average [CO_3^{2-}] during the later interval. Several notable [CO_3^{2-}] events recorded in our proxy record coincide with low [CO_3^{2-}] outputs in SBB model simulations[20] and occur in association with the timing of several strong El Niño events (1982–1983, 1987–1988, 1997–1998).

By applying the ANSW–[CO_3^{2-}] relationship presented by Osborne et al[29]. to our downcore ANSW measurements, we estimate that surface ocean [CO_3^{2-}] in the SBB decreased by 35%, representing a net change of approximately $98\pm 16\,\mu mol\,kg^{-1}$ in [CO_3^{2-}] over the twentieth century (from $271\pm 16\,\mu mol\,kg^{-1}$ in 1895 to $173\pm 16\,\mu mol\,kg^{-1}$ in 2000; Fig. 2). Recent in situ surface ocean [CO_3^{2-}] measurements from the SBB in the NOAA's WCOA data (2011–2013) and taken by CalCOFI (2009–2015) are in excellent agreement with the forward-projected trend of our estimated [CO_3^{2-}] values, even though these datasets do not temporally overlap. The time-series slopes, used to determine a decadal rate of change, recorded by our proxy reconstruction ($-9.992\,\mu mol\,kg^{-1}\,dec^{-1}$) and the integrated CalCOFI and WCOA data ($-10.716\,\mu mol\,kg^{-1}\,dec^{-1}$) are within error of one another. An additional comparison to the HOT dataset from the North Pacific[33] also shows a similar long-term decline ($-6.616\,\mu mol\,kg^{-1}\,dec^{-1}$), albeit with significantly higher [CO_3^{2-}] values and a lower rate of decline, illustrating the inherently low [CO_3^{2-}] conditions in the CCE. Hindcast model simulations for the CCE indicate a long-term trend (-5.431, -5.397 and $-4.949\,\mu mol\,kg^{-1}\,dec^{-1}$ at 0, 30 and 50 m depth, respectively) that is also in agreement with our proxy record; however, simulations indicate overall lower rate of change and [CO_3^{2-}] values relative to our ANSW-based estimates, which is probably a result of negative biases that exist in the model configuration employed (refs. [20,22], see Methods).

As the relative concentrations of the dissolved inorganic carbon (DIC) species in seawater (CO_2, HCO_3^-, CO_3^{2-}) covary in a predictable way, so do the variables of the marine carbonate system (DIC, total alkalinity (TA), pH and the partial pressure of CO_2. We use an

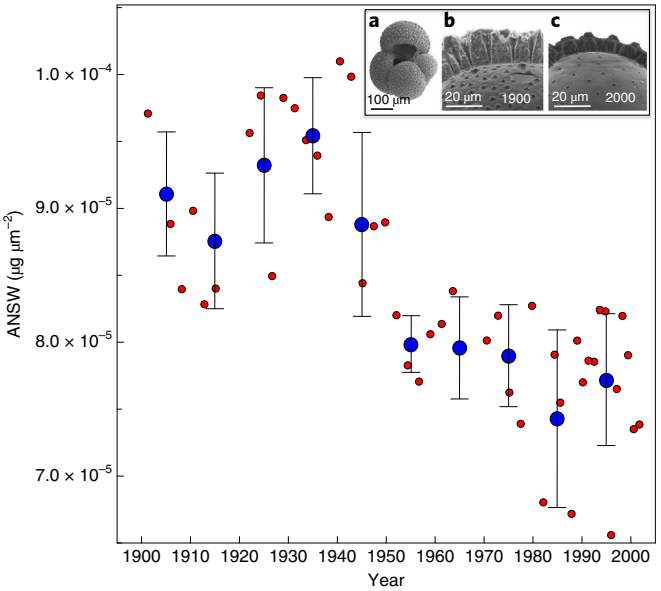

Fig. 1 | Decadal population mean ANSW. Red circles show the sample averages for the 58 sediment slices examined in this study. Decadal mean time-slice populations (blue circles) of *G. bulloides* ANSW show a significant offset in the shell thicknesses measured in 1900–1910 and 1990–2000. Error bars show the 95% confidence intervals. **a**–**c**, SEM images show a typical *G. bulloides* specimen from the SBB (**a**) and shell wall cross-sections of similarly sized shells from the upper- (**b**) and lower-most (**c**) samples of the box core, clearly illustrating the difference in shell wall thickness over the past century.

empirical salinity–TA relationship derived for the coastal zone of the CCE and sea surface salinity measurements from the Scripps Pier (1916–present) time series to estimate TA for our record[34]. No salinity observations exist for the period 1895–1915; a best-fit linear regression is therefore used to estimate salinity values for those years. As this approach incorporates a great deal of uncertainly, particularly when applied to the palaeo record, we use a combination of our downcore proxy-[CO_3^{2-}] and a salinity–TA estimates to roughly characterize the full carbonate system to report how the most commonly used measure of OA, pH, has evolved over the last century, so it can be compared with other published results (see Methods). These estimates indicate that the [H^+] of seawater has increased by 80%, translating into a 0.21 unit decline in pH that exceeds the global average of 0.1 units by more than a factor of two[35]. We do not report the error for this estimate, as a number of assumptions were made for these calculations and a reported value would probably underestimate uncertainty. However, our calculated decadal rate of pH decline for this region over the past century ($-0.021\,dec^{-1}$) is consistent with the rate of pH decline modelled for the entire CCE ($-0.020\,dec^{-1}$; 1979–2012[20]) and larger-scale observations for the North Pacific ($-0.017\,dec^{-1}$ from 1991–2006[36] and $-0.019\,dec^{-1}$ from 1988–2014; refs. [33,37]). Our results are also consistent with large declines in pH resulting from strong upwelling, as is depicted by regional model simulations for the central region of the CCE[20,21].

Disentangling drivers of ocean acidification

The surface ocean carbonate system in our study region is influenced by a combination of exposure to atmospheric CO_2, the local introduction of waters with low [CO_3^{2-}] via shifts in upwelling and surface circulation, and local changes in productivity. To evaluate the dominating mechanism(s) driving the twentieth-century changes in the upper water column carbonate system, we use the

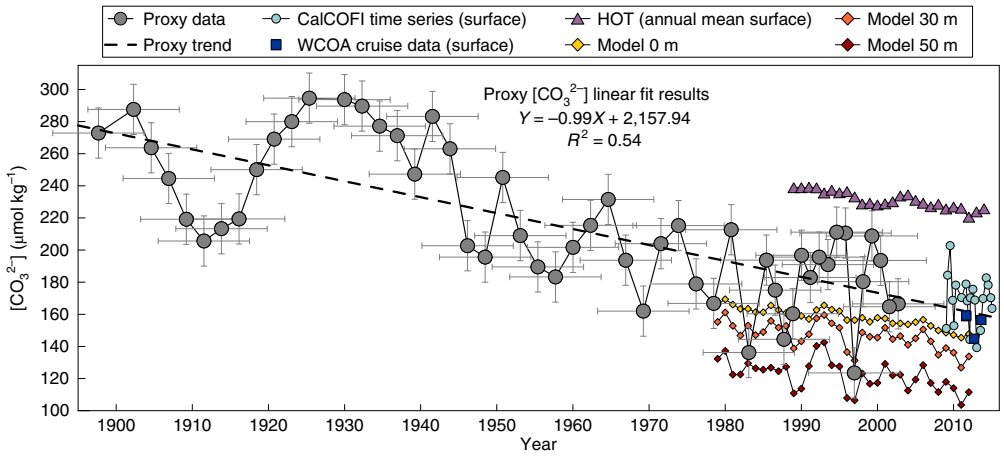

Fig. 2 | Twentieth-century proxy [CO_3^{2-}] record based on *G. bulloides* ANSW for the period 1895–2000. Horizontal error bars represent age uncertainty (±6 yr) and vertical error bars (±15.63 μmol kg^{-1}) represent the standard error of the estimate of [CO_3^{2-}] associated with the calibration relationship[29]. Proxy data are compared with model simulations (1979–2012 (ref. [20])), in situ measurements from the Santa Barbara Basin[17] and HOT data from the North Pacific[33]. The average modern [CO_3^{2-}] is 164 μmol kg^{-1} and temperature is 15 °C, based on 2010–2015 in situ data.

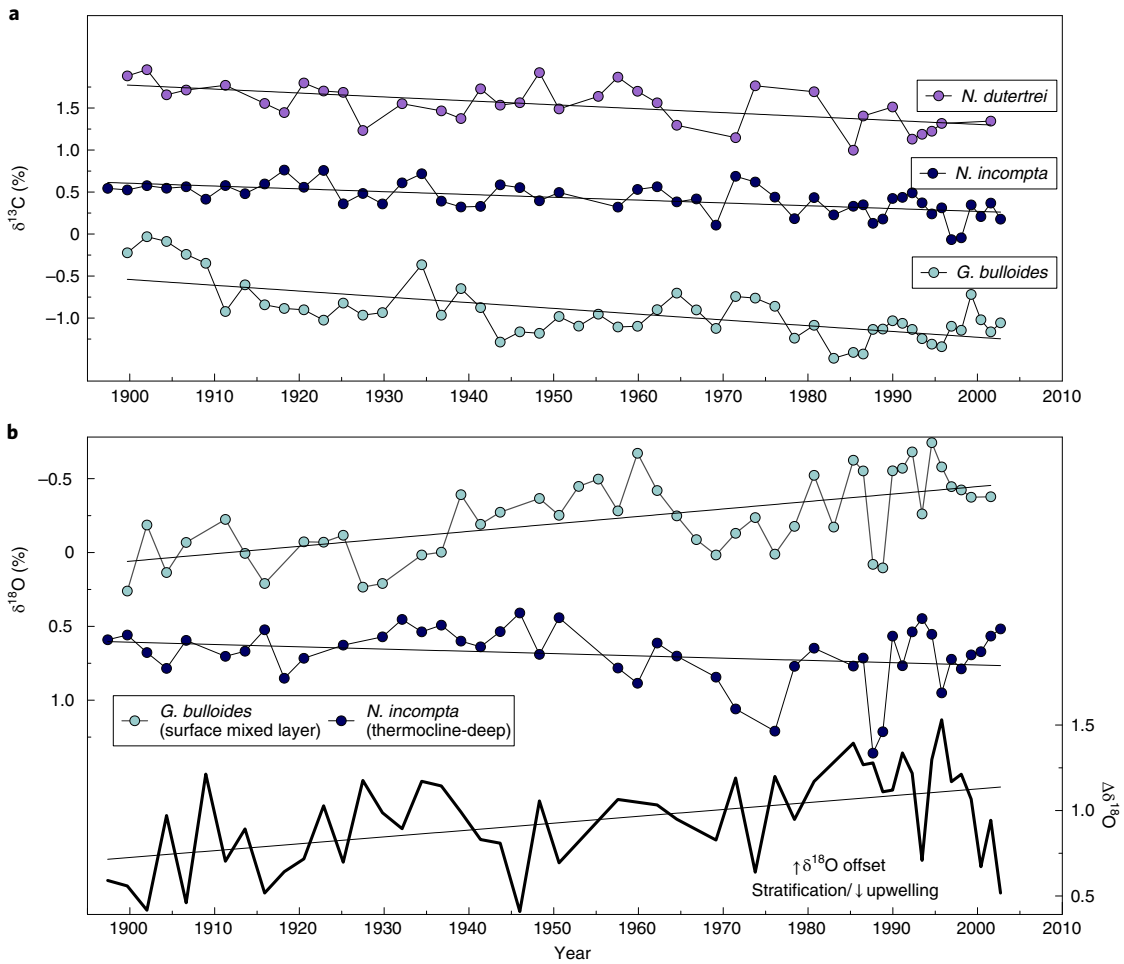

Fig. 3 | Stable isotope tracers of influential processes. a, The $\delta^{13}C$ records of three planktonic foraminifera species (*G. bulloides, N. incompta and N. dutertrei*; $R^2 = 0.46$, 0.36 and 0.34, respectively, $P < 0.005$), showing a long-term decline consistent with an increasing anthropogenic CO_2 inventory in the surface ocean. **b**, The $\delta^{18}O$ records of *G. bulloides* (surface-mixed-layer-dwelling species) and *N. incompta* (thermocline-deep-dwelling species) (top), and the difference between the two records ($\Delta\delta^{18}O$) (bottom), which are used to trace the relative depth habitats and as a proxy for changes in the depth of the thermocline and the related thickness and stability of the mixed layer[45]. $\delta^{18}O$ values are relative to the Vienna PeeDee Belemnite.

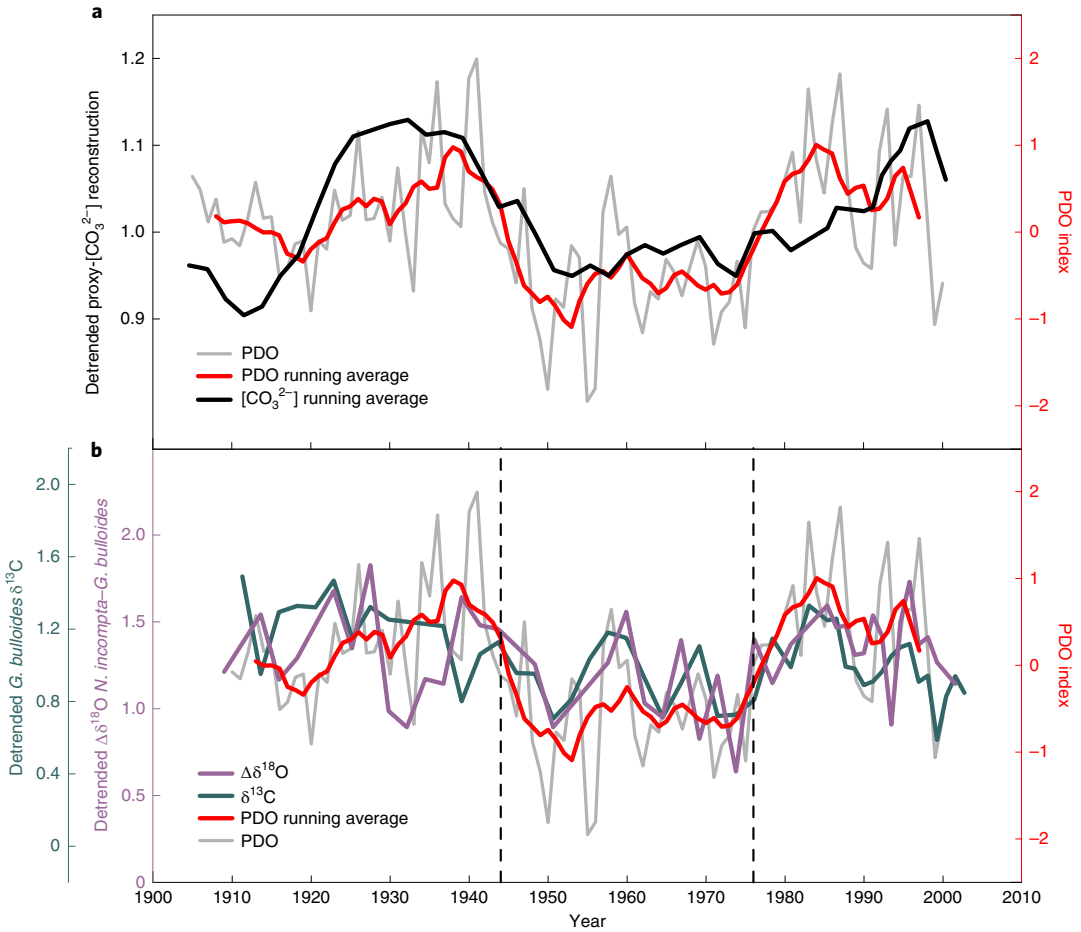

Fig. 4 | Linking upwelling strength, the PDO and carbonate system state. a, The $[CO_3^{2-}]$ record is shown, with the long-term, anthropogenically driven decline removed (detrended) plotted with the PDO index[48]. An apparent correlation between high/low $[CO_3^{2-}]$ and positive/negative PDO phases is evident. Both datasets are shown as 5 yr running means. **b**, The detrended $\Delta\delta^{18}O$ (*N. incompta*–*G. bulloides*) and *G. bulloides* $\delta^{13}C$ are shown to highlight the natural variability not associated with anthropogenic ocean acidification, plotted again with the PDO index, indicating a relationship between weakened/strengthened upwelling and positive/negative PDO phases.

downcore foraminiferal stable isotopic records as tools to track carbon source and water column structure.

The $\delta^{13}C$ record of *G. bulloides* and two other foraminifera species (*Neogloboquadrina incompta and Neogloboquadrina dutertrei*) sampled from the core show significant ($R^2 = 0.46$, 0.36 and 0.34, respectively $P < 0.005$) long-term declines in $\delta^{13}C$ (Fig. 3). The observed increase in the surface ocean inventory of anthropogenic carbon sourced from ^{12}C-enriched fossil fuels causes an overall decline in the $\delta^{13}C$ of seawater: a globally observed phenomenon termed the the Suess Effect[38,39]. Variability in local productivity and upwelling of DIC- and ^{12}C-rich intermediate- and deep-water (from respiration and remineralization) could also influence the surface ocean, and (by extension) foraminiferal $\delta^{13}C$. The observed long-term decline in $\delta^{13}C$ is consistent with an increase in ^{13}C-depleted anthropogenic CO_2, stemming primarily from uptake from the atmosphere, strengthened upwelling, a decline in productivity or a combination of these processes.

A $[CO_3^{2-}]$ effect has been observed in the stable isotope signatures recorded by foraminifera, whereby elevated $[CO_3^{2-}]$ results in relatively lower $\delta^{13}C$ (ref. [27]). Considering the $[CO_3^{2-}]$ effect on foraminiferal $\delta^{13}C$, we estimate, on the basis of the culture-derived relationship of Spero et al.[27] for 13-chambered *G. bulloides* and the change in $[CO_3^{2-}]$ estimated by our proxy record, that $\delta^{13}C$ would increase by 0.94‰ from the years 1895 to 2000, whereas the measured decrease is −0.72‰. This modelled change in the opposite direction is consistent with other, similar studies, and suggests that the magnitude of foraminiferal $\delta^{13}C$ depletion may actually be much larger when the $[CO_3^{2-}]$ effect is removed[40].

Considering the influence of upwelling on our $\delta^{13}C$ record, a majority of model evidence for the CCE suggests that coastal upwelling will be enhanced in coastal eastern boundary upwelling systems (EBUS) due to the climate-induced strengthening of alongshore winds that drive Ekman upwelling (for example, see ref[41]). However, historical observations from the CalCOFI time series (1950–present) in the SBB report stratifying conditions over the latter half of the twentieth century associated with warming sea surface temperatures, deepening of the thermocline depth and declining zooplankton biomass[42–44]. Using the $\Delta\delta^{18}O$–water column structure proxy, we compare $\delta^{18}O$ signatures recorded by the surface-mixed-layer species (*G. bulloides*) with the thermocline to deep-dwelling foraminifera species (*N. incompta*) to infer the depth of the thermocline and the stability of the mixed layer[45]. The observed increase in $\Delta\delta^{18}O$ represents an increasing offset in depth habitat and therefore a decline in upwelling strength, providing further evidence of twentieth-century CCE stratification, which would hypothetically result in an increase in $\delta^{13}C$ over our record, rather than the observed decrease (Fig. 3).

Shifts in dinoflagellate cyst assemblages in the SBB also suggest a reduction in upwelling and shed light on an overall reduction in seasonal primary productivity throughout the twentieth century[46].

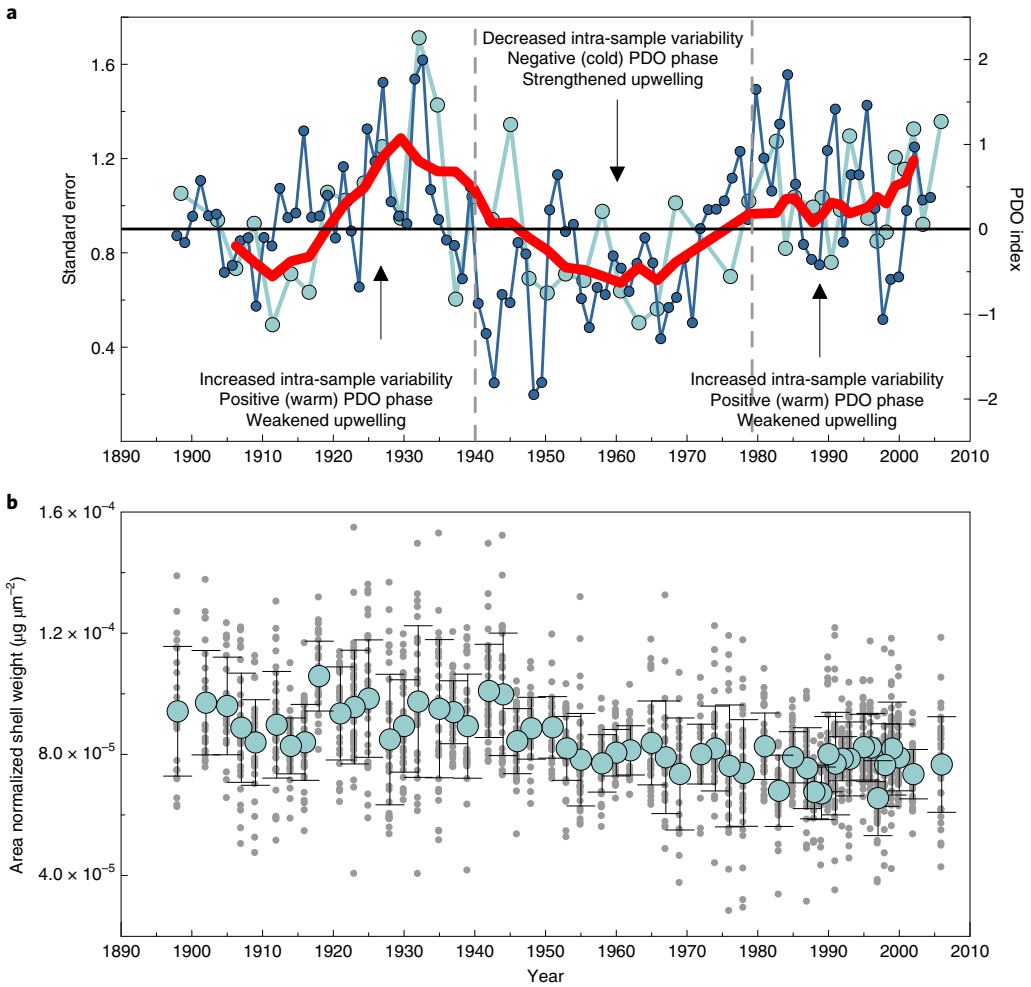

Fig. 5 | Using individuals to trace habitat depth and upwelling strength. a, Time series showing the sample ANSW standard error plotted ($\sigma/\sqrt{n}$) (n, sample size) with the PDO index. These time series show increased variability associated with positive PDO phases that are marked by weakened upwelling strength. The solid horizontal line correlates with the PDO index (right, y-axis) and delineates the threshold between positive and negative phases of PDO. Vertical dashed lines mark the temporal transitions between positive and negative phases of PDO based on the PDO index. **b**, Individual ANSW measurements (grey circles) plotted with sample average ANSW (blue circles) and associated sample standard error bars.

While this reduction in productivity is consistent with the sign of our $\delta^{13}C$ record, we argue that the magnitude of the productivity change is not great enough to persistently drive the observed $\delta^{13}C$ record. Productivity in the CCE and other EBUS may instead be a synergistic factor and important on shorter timescales.

Collectively, our records indicate that the increasing surface ocean inventory of anthropogenic CO_2 is the dominant long-term control on $\delta^{13}C$, and by extension $[CO_3^{2-}]$, recorded in our proxy record. This is supported by the fact that owing to a relatively robust scaling between the ^{13}C Suess effect and the increase in anthropogenic CO_2 of about −0.017 permil (μmol kg^{-1})$^{-1}$[147], the long-term decrease in $\delta^{13}C$ of about 0.72‰ over the 1895 to 2000 period implies an increase in anthropogenic CO_2 of about 42 μmol kg^{-1}. This is slightly smaller than the expected increase of about 50 μmol kg^{-1} over this period, but supports our conclusion of a dominant contribution of the uptake of anthropogenic CO_2 to our reconstructed decrease in $[CO_3^{2-}]$.

Decadal-scale variability

While we attribute the long-term reduction in $[CO_3^{2-}]$ largely to air–sea exchange of anthropogenic CO_2, considerable variability exists around the declining trend. To better visualize this variability, we detrended the $[CO_3^{2-}]$ record, revealing decadal- and subdecadal- scale oscillations that are significantly correlated with the Pacidic Decadal Oscillation (PDO) index[48] ($R^2 = 0.53$, $P < 0.005$; Extended Data Fig. 5) (Fig. 4). During positive (warm) phases of the PDO the carbonate system shifts to a higher $[CO_3^{2-}]$ state, whereas negative (cool) phases of the PDO coincide with overall lower $[CO_3^{2-}]$ values (Fig. 4a). PDO is associated with decadal-scale changes in the strength of the Aleutian Low, resulting in basin-wide temperature, pressure and wind stress anomalies in the Pacific Ocean[49]. Within the CCE, the positive phase of the PDO coincides with weaker Aleutian Low winds, resulting in decreased coastal upwelling, warmer sea surface temperatures and reduced productivity. Conversely, the negative phase of the PDO produces the opposite set of conditions.

As coastal upwelling controls the amount of low-pH, CO_2-rich water that reaches the surface, and PDO regulates the strength of upwelling, we hypothesize that this mechanism alters the surface carbonate system on decadal timescales. El Niño and La Niña events, typically lasting 6–18 months, produce similar anomalies and have already been observed in association with sustained changes in coastal upwelling and the acidity of surface waters off the continental shelf of California[50].

We use our detrended stable isotopic records ($\delta^{13}C$ and $\Delta\delta^{18}O$) to evaluate the variability occurring independently of the long-term

trend. We find that residual trends in $\delta^{13}C$ and $\Delta\delta^{18}O$ covary with the PDO: positive phases are marked by a higher $\Delta\delta^{18}O$ and $\delta^{13}C$ signatures, which represent decreased upwelling/increased stratification and warmer temperatures (Fig. 4). We also use the individual calcification response to assess upwelling variability on the basis of a similar foraminiferal depth habitat premise to the $\Delta\delta^{18}O$ proxy. During periods of strengthened upwelling, less intrasample variability is expected for a given *G. bulloides* population, since a shoaled thermocline would tighten the suitable habitable depth range for this species above the thermocline to the sea surface. The opposite would be true for stratified conditions. Using the sample population standard error as a measure of intrasample variability, a greater spread in individual ANSW is shown to be associated with intervals of positive PDO marked by weaker upwelling relative to negative PDO phases, when stronger upwelling occurs ($R^2 = 0.55$, $P < 0.005$, Fig. 5 and Extended Data Fig. 5). Together, these proxy records corroborate that as upwelling weakens in the CCE during positive PDO phases, higher $[CO_3^{2-}]$ levels occur and during negative phases of the PDO, strengthened upwelling produces persistently lower $[CO_3^{2-}]$ conditions.

Implications for future ocean acidification

Our ocean acidifcation reconstruction indicates a significant long-term decline in $[CO_3^{2-}]$ of 35% recorded for the central CCE over the twentieth century as a result of increasing concentrations of anthropogenic CO_2 in seawater. Our ocean acidifcation record reveals considerable variability around this long-term trend, which we find to be significantly correlated with decadal-scale changes in upwelling strength associated with the PDO. This implies that over decadal timescales, the positive/negative phases of the PDO coincide with an overall elevated/reduced $[CO_3^{2-}]$ state as a result of shifts in upwelling strength. The relationship between the PDO and ocean acidifcation means that the anthropogenic acidification signal will be both amplified and alleviated in response to decadal shifts in the PDO phase, suggesting that that future progression of ocean acidification will be substantially modulated by large-scale climate modes. While projections of $[CO_3^{2-}]$ are important for understanding how the system may progress in the future, our past record indicates that $[CO_3^{2-}]$ will not decline linearly and that climatic forcing will be important in the coming century.

Online content

Any methods, additional references, Nature Research reporting summaries, source data, extended data, supplementary information, acknowledgements, peer review information; details of author contributions and competing interests; and statements of code and data availability are available at https://doi.org/10.1038/s41561-019-0499-z.

Received: 17 June 2019; Accepted: 6 November 2019;
Published online: 16 December 2019

References

1. Lüthi, D. et al. High-resolution carbon dioxide concentration record 650,000–800,000 years before present. *Nature* **453**, 379–382 (2008).
2. Feely, R. A. et al. Impact of anthropogenic CO_2 on the $CaCO_3$ system in the oceans. *Science* **305**, 362–366 (2004).
3. Orr, J. C. et al. Anthropogenic ocean acidification over the twenty-first century and its impact on calcifying organisms. *Nature* **437**, 681–686 (2005).
4. Gruber, N. et al. The ocean sink for anthropogenic CO_2 from 1994 to 2007. *Science* **363**, 1193–1199 (2019).
5. Khatiwala, S. et al. Global ocean storage of anthropogenic carbon. *Biogeosciences* **10**, 2169–2191 (2013).
6. Le Quéré, C. et al. Global carbon budget 2015. *Earth Syst. Sci. Data* **7**, 349–396 (2015).
7. Bednaršek, N. et al. New ocean, new needs: application of pteropod shell dissolution as a biological indicator for marine resource management. *Ecol. Indic.* **76**, 240–244 (2017).
8. de Moel, H. et al. Planktic foraminiferal shell thinning in the Arabian Sea due to anthropogenic ocean acidification? *Biogeosciences* **6**, 1917–1925 (2009).
9. De'ath, G., Lough, J. M. & Fabricius, K. E. Declining coral calcification on the Great Barrier Reef. *Science* **342**, 116–119 (2009).
10. Fabry, V. J., Seibel, B. A., Feely, R. A. & Orr, J. C. Impacts of ocean acidification on marine fauna and ecosystem processes. *ICES J. Mar. Sci.* **65**, 414–432 (2008).
11. Meier, K. J. S., Beaufort, L., Heussner, S. & Ziveri, P. The role of ocean acidification in *Emiliania huxleyi* coccolith thinning in the Mediterranean Sea. *Biogeosciences* **11**, 2857–2869 (2014).
12. Moy, A. D., Howard, W. R., Bray, S. G. & Trull, T. W. Reduced calcification in modern Southern Ocean planktonic foraminifera. *Nat. Geosci.* **2**, 276–280 (2009).
13. Ries, J. B., Cohen, A. L. & McCorkle, D. C. Marine calcifiers exhibit mixed responses to CO_2-induced ocean acidification. *Geology* **37**, 1131–1134 (2009).
14. Rivero-Calle, S., Gnanadesikan, A., Del Castillo, C. E., Balch, W. M. & Guikema, S. D. Multidecadal increase in North Atlantic coccolithophores and the potential role of rising CO_2. *Science* **350**, 1533–1537 (2015).
15. Iglesias-Rodriguez, D. et al. Phytoplankton calcification in a high-CO_2 world. *Science* **320**, 336–340 (2008).
16. Feely, R. A., Sabine, C. L., Hernandez-Ayon, J. M., Ianson, D. & Hales, B. Evidence for upwelling of corrosive 'acidified' water onto the continental shelf. *Science* **320**, 1490–1492 (2008).
17. Feely, R. A. et al. Chemical and biological impacts of ocean acidification along the west coast of North America. *Estuar. Coast. Shelf Sci.* **183**, 260–270 (2016).
18. Feely, R. A. et al. The combined effects of acidification and hypoxia on pH and aragonite saturation in the coastal waters of the Californian Current Ecosystem and the northern Gulf of Mexico. *Cont. Shelf Res.* **152**, 50–60 (2018).
19. Hauri, C. et al. Ocean acidification in the California Current System. *Oceanography* **22**, 60–71 (2009).
20. Turi, G., Lachkar, Z., Gruber, N. & Munnich, M. Climatic modulation of recent trends in ocean acidification in the California Current System. *Environ. Res. Lett.* **11**, 014007 (2016).
21. Gruber, N. et al. Rapid progression of ocean acidification in the California Current System. *Science* **337**, 220–223 (2012).
22. Hauri, C., Gruber, N., McDonnell, A. M. P. & Vogt, M. The intensity duration and severity of low aragonite saturation state events on the California continental shelf. *Geophys. Res. Lett.* **40**, 3424–3429 (2013).
23. Bednaršek, N. et al. *Limacina helicina* shell dissolution as an indicator of declining habitat suitability due to ocean acidification in the California Current Ecosystem. *Proc. R. Soc. Lond. B* **281**, 20140123 (2014).
24. Takahashi, T., Williams, R. T. & Bos, D. L. in *GEOSECS Pacific Expedition Volume 3: Hydrographic Data 1973–1974* (eds Broecker, W. S. et al.) 77–83 (National Science Foundation, 1982).
25. Barker, S. & Elderfield, H. Foraminiferal calcification response to glacial-interglacial changes in atmospheric CO_2. *Science* **297**, 833–836 (2002).
26. Bijma, J., Spero, H. J. & Lea, D. W. in *Use of Proxies in Paleoceanography: Examples from the South Atlantic* (eds Fisher, G. & Wefer, G.) 489–512 (Springer, 1999).
27. Spero, H. J., Bijma, J., Lea, D. W. & Bemis, B. E. Effect of seawater carbonate concentration on foraminiferal carbon and oxygen isotopes. *Nature* **390**, 497–500 (1997).
28. Marshall, B. J., Thunell, R., Hennehan, M., Astor, Y. & Wejnert, K. Planktonic foraminiferal area density as a proxy for carbonate ion concentration: a calibration study using the Cariaco Basin ocean time series. *Paleoceanography* **28**, 363–376 (2013).
29. Osborne, E. B. et al. Calcification of the planktonic foraminifera *Globigerina bulloides* and carbonate ion concentration: results from the Santa Barbara Basin. *Paleoceanography* **31**, 1083–1102 (2016).
30. Aldridge, D., Beer, C. J. & Purdie, D. A. Calcification in the planktonic foraminifera *Globigerina bulloides* linked to phosphate concentrations in surface waters of the North Atlantic Ocean. *Biogeosciences* **9**, 1725–1739 (2012).
31. Beer, C. J., Schiebel, R. & Wilson, P. A. Testing planktic foraminiferal shell weight as a surface water $[CO_3^{2-}]$ proxy using plankton net samples. *Geology* **38**, 103–106 (2010).
32. De Villiers, S. Optimum growth conditions as opposed to calcite saturation as a control on the calcification rate and shell-weight of marine foraminifera. *Mar. Biol.* **144**, 45–49 (2004).
33. Dore, J. E., Lukas, R., Sadler, D. W., Church, M. J. & Karl, D. M. Physical and biogeochemical modulation of ocean acidification in the central North Pacific. *Proc. Natl Acad. Sci. USA* **106**, 12235–12240 (2009).
34. Fassbender, A. J. et al. Estimating total alkalinity in the Washington State Coastal Zone: complexities and surprising utility for ocean acidification research. *Estuar. Coasts* **40**, 404–418 (2016).
35. Caldeira, K. & Wickett, M. E. Anthropogenic carbon and ocean pH. *Nature* **425**, 365 (2003).

36. Byrne, R. H., Mecking, S., Feely, Ra. & Liu, X. Direct observations of basin-wide acidification of the North Pacific Ocean. *Geophys. Res. Lett.* **37**, L02601 (2010).
37. Bates, N. et al. A time-series view of changing ocean chemistry due to ocean uptake of anthropogenic CO_2 and ocean acidification. *Oceanography* **27**, 126–141 (2014).
38. Gruber, N. et al. Spatiotemporal patterns of carbon-13 in the global surface oceans and the oceanic Suess effect. *Glob. Biogeochem. Cycles* **13**, 307–335 (1999).
39. Keeling, C. D. The Suess effect: ^{13}carbon-^{14}carbon interrelations. *Environ. Int.* **2**, 229–300 (1979).
40. Black, D., Thunell, R. C., Wejnert, K. & Astor, Y. Carbon isotope composition of Caribbean sea surface waters: response to the uptake of anthropogenic CO_2. *Geophys. Res. Lett*. https://doi.org/10.1029/2011GL048538 (2011).
41. Sydeman, W. J. et al. Climate change and wind intensification in coastal upwelling ecosystems. *Science* **345**, 77–80 (2014).
42. Di Lorenzo, E., Miller, A. J. & SchneiderNand McWilliams, J. C. The warming of the California Current System: dynamics and ecosystem implications. *J. Phys. Oceanogr.* **35**, 336–362 (2005).
43. McGowan, J., Bograd, S., Lynn, R. J. & Miller, A. J. The biological response to the 1977 regime shift in the California Current. *Deep Sea Res. Pt II* **50**, 2567–2582 (2003).
44. Roemmich, D. & McGowan, J. Climatic warming and the decline of zooplankton in the California Current. *Science* **267**, 1324–1326 (1995).
45. Pak, D. K. & Kennett, J. P. A foraminiferal isotopic proxy for upper water mass stratification. *J. Foram. Res.* **32**, 319–327 (2002).
46. Bringue, M., Pospelova, V. & Field, D. B. High resolution sedimentary record of dinoflagellate cysts reflects decadal variability and 20th century warming in the Santa Barbara Basin. *Quat. Sci. Rev.* **105**, 86–101 (2014).
47. Sonnerup, R. E. & Quay, P. D. ^{13}C constraints on ocean carbon cycle models. *Glob. Biogeochem. Cycles* **26**, GB2014 (2012).
48. Hare, S. R. *Low Frequency Climate Variability and Salmon Production.* PhD thesis, Univ. Washington (1996).
49. Mantua, N. J. & Hare, S. R. The Pacific Decadal Oscillation. *J. Oceanogr.* **58**, 35–44 (2002).
50. Nam, S., Kim, H.-J. & Send, U. Amplification of hypoxic and acidic events by La Niña conditions on the continental shelf off California. *Geophys. Res. Lett.* **120**, 5387–5399 (2015).

Publisher's note Springer Nature remains neutral with regard to jurisdictional claims in published maps and institutional affiliations.

This is a U.S. government work and not under copyright protection in the U.S.; foreign copyright protection may apply 2019

Methods

ANSW. While several shell weight size-normalization techniques used to estimate foraminiferal calcification and shell thickness exist, we chose to use ANSW, which uses individual (rather than bulk) population measurements[28]. This method is currently the most effective size-normalization technique (compared with measure-based weights and sieve-based weights) that best constrains shell thickness[28,29]. The inability to effectively size-normalize shell weight measurements results in datasets that are influenced not only by CO_3^{2-} but also by temperature, as temperature results in larger and heavier shells but has no effect on shell thickness. See Osborne et al.[29] for an in-depth discussion and review of previously published results for this species.

We aimed to pick 40 individual *G. bulloides* shells from the >150 μm size-fraction of each sediment sample for ANSW analyses. On average, 35 individuals are included in each ANSW data point (maximum 40 and minimum 17 individuals), representing a total of 1,870 analysed shells included in this dataset. Individual *G. bulloides* shells with abnormally formed shells or visible clay and/or organic material were excluded from our analyses, as these characteristics could effect weight and area measurements. The presence of an encrusted cryptic morphospecies of *G. bulloides* has been documented in the Santa Barbara Channel[51–53]. Further investigation indicated that the less-abundant and cool-water-loving 'encrusted' morphospecies calcifies and fractionates stable carbon and oxygen isotopes differently to the more-abundant 'normal' morphospecies[29,51]. Owing to the offset in ANSW and the intention to use these *G. bulloides* shells for later stable isotope analyses, morphometric measurements collected during ANSW processing are also used to identify and remove encrusted individuals from our sample populations (refs. [29,54]). The species-specific ANSW response of the normal *G. bulloides* morphospecies to ambient $[CO_3^{2-}]$ has been constrained using individuals collected in the SBB by a sediment trap time series (equation (2)). Stable isotope results from this 3.5 yr sediment-trap analysis indicate that, on average, *G. bulloides* calcifies in the 40 m depth range, although seasonal variability in depth habit does occur in association with upwelling.

While there can still be a considerable amount of variability within a single sediment sample, statistical analyses by Osborne et al[29]. demonstrate the asymptotic nature of the per cent error as a function of the numbers of individuals used in an ANSW measurement. These results suggest that a pool of 30–40 individuals represents a high degree of confidence when using a mean area density value to represent the population mean. Each shell is individually weighed in a copper weigh boat using a high-precision microbalance (Mettler Toledo XP2U, ±0.43 μg) in an environmentally controlled weigh room. Next, each individual is photographed positioned umbilical side up using a binocular microscope (Zeiss Stemi 2000-C) fitted with a camera (Point Grey Research Flea3 1394b). A microscopic imaging program (Orbicule Macnification 2.0) was used to analyse shells photos for length (Feret diameter) and the two-dimensional surface area or silhouette. Macnification 2.0 program the RGB images to calculate a region of interest and generates an outline of the shell image, which is then used to estimate a pixel two-dimensional area. Pixel measurements are converted to lengths (μm) and areas (μm²) by calibrating an image of a 1 mm microscale taken at the same magnification and working distance as the shell photos. Individual shell weights were then divided by their corresponding areas and a mean ANSW value was calculated for each sample population. These ANSW values were then applied to the calibration relation relationship (equation (1)) presented by Osborne et al.[29] to estimate $[CO_3^{2-}]$.

$$\left[CO_3^{2-}\right] = \left(\mathrm{ANSW} - 4.19\times10^{-5}\right)/1.92\times10^{-7} \quad (1)$$

Age model development. Approximately 2 g from each sample were freeze-dried and used for radioisotope measurements. Wet weights (recorded before freeze-drying) and dry weights were used to estimate the sample porosity and correct for compaction. Freeze-dried sediments were ground, loaded into counting vials and sealed with epoxy for 3 weeks before counting. Each sample was measured (3–5 days) for ^{210}Pb, ^{214}Pb and ^{137}Cs via gamma-decay counting using a high-purity germanium well detector[55].

The excess ^{210}Pb ($^{210}Pb_{ex}$), reflective of atmospheric deposition, rather than supported ^{210}Pb ($^{210}Pb_{supp}$) from the decay of ^{226}Ra, was determined by subtracting the activity of ^{214}Pb (assumed to be in secular equilibrium with $^{210}Pb_{supp}$; mean 3.7 dpm g^{-1}) from the activity of ^{210}Pb. The exponential decay of $^{210}Pb_{ex}$ observed in the core sediments (Fig. 3) was used to determine ages for the core using a combination of constant initial concentration (CIC) and constant rate of ^{210}Pb supply (CRS) models. An offset of approximately ±1 yr was observed between models. Using these age constraints, an average sedimentation rate of 0.43 cm yr^{-1}, and an average mass accumulation rate of 5.84 g cm^{-2} yr^{-1}, were determined for the core. The sedimentation rate determined from the $^{210}Pb_{ex}$ is relatively uniform over the entire 0.5 m core and is also in good agreement with previously determined radioisotope chronologies for the SBB[56–58]. The increase in ^{137}Cs activity at 19 cm (Fig. 3) is used as an independent age marker horizon for the year 1964, and represents the peak in radioactive fallout from atmospheric nuclear bomb testing[59,60]. The depth of the ^{137}Cs spike was shallower than expected using both the CRS and CIC models when assuming a 2012 collection year as the core-top age. We therefore conclude that the upper several centimetres of sediments were not preserved when this box core was collected. As such, we applied a 6 yr age correction, which is also used as the age error estimate, and anchored the 19 cm ^{137}Cs spike to a depositional year of 1964. These age constraints indicate that the 0.5 m core extends back to ~1895 and that the uppermost sediments contained in the core represent the year ~2006.

CCE marine carbonate system model simulation. The model-based estimates of the progression of the $[CO_3^{2-}]$ in the SBB stem from the simulations described in detail by Turi et al.[20]. Annual mean data were extracted from the model at the four nearest gridpoints to the location of the core from various depths (0 m, 30 m, and 50 m). The model is based on the UCLA-ETH version of the Regional Oceanic Modeling System[61], and includes a nitrogen-based nutrient–phytoplankton zooplankton–detritus model[62] that was extended with a carbon module[63,64]. The CalCS model setup employed here has a horizontal resolution of 5 km and 34 levels in the vertical, spans the entire US coast from about 30° N to 50° N and extends more than 1,300 km into the Pacific. The hindcast simulation (1979–2012) was forced at the surface with fluxes of heat and freshwater from ECMWF's ERA-Interim reanalysis[65]. The boundary conditions at the lateral boundaries of the model consisted of a combination of climatological fields based on observations and time-varying anomaly fields derived from a global hindcast simulation with theNCAR CCSM3 model[66]. The evaluation of the model simulated pH and Ω_{arag} with observations revealed that the model is capturing the large-scale offshore and depth gradients very well, but that it has a slight positive bias in the nearshore regions north of Point Conception[22]. Owing to the lack of in situ measurements from the SBB, no assessment could be undertaken in this part of the CalCS, but the comparison with the time-series records from Santa Monica Bay[67] suggests a slight overestimation of the modelled pH and Ω_{arag} in the upper ocean.

Stable isotope measurements. At least 100 μg (30–40 individuals) of *G. bulloides* used for ANSW analyses were pooled to measure the stable $\delta^{18}O$ and $\delta^{13}C$ isotopic compositions. Foraminifera were cleaned for 30 min in 3% H_2O_2 followed by a brief sonication and acetone rinse before analysis. Stable isotope measurements were carried out on an Isoprime isotope ratio mass spectrometer equipped with a carbonate preparation system. The long-term standard reproducibility is 0.07‰ for $\delta^{18}O$ and 0.06‰ for $\delta^{13}C$. Results are reported relative to the Vienna Pee Dee Belemnite.

Marine carbonatesystem calculations. Carbonate system variables for the historic record were determined using the CO2Sys Program (version 2.1). TA and DIC were used as master input variables (equations (2) and (3)) and in situ measurements of sea surface temperature and salinity as input conditions when data are available (Shore Stations Program). Sea surface salinity measurements from the Scripps Pier (1916–present) located just south of our study region and sea surface temperature measurements from the SBB (1955–present) were used for our calculations. A comparison of more recent salinity measurements from the SBB and Scripps Pier indicate that salinity values in these two regions are comparable. For the period 1916–1954, when SST was not measured in the SBB but was measured at Scripps Pier, we use an average offset between the overlapping periods of these datasets (1955–1900) to extrapolate an SST for the SBB. For the period 1900–1916 when there is no hydrographic data available, we use the time-integrated relationship for temperature and salinity to estimate these parameters.

We solve for our input master variables (TA and DIC) by coupling proxy $[CO_3^{2-}]$ estimates and a salinity-based estimate of TA[34]. Although this salinity–alkalinity relationship was derived using carbonate system measurements for the coastal Oregon CCE, a compilation of CalCOFI data from the SBB yields a relationship that is within error of the published Fassbender et al[34]. dataset. We also incorporate total boron into our estimate of TA, which was determined using the R program seacarb (Total Boron Package[68]). To estimate DIC, we sum the estimated $[CO_3^{2-}]$ with the derived $[HCO_3^-]$ and assume that any concentration of CO_2 is less than 1% of DIC (ref. [69]; equation (3)).

$$\mathrm{TA} = \left[HCO_3^-\right] + 2\left[CO_3^{2-}\right] + \left[B(OH)_4^-\right] \quad (2)$$

$$\mathrm{DIC} = \left[HCO_3^-\right] + \left[CO_3^{2-}\right] \quad (3)$$

Data availability

The authors declare that the data supporting the findings of this study are available within the article. New data generated as a part of this study have been made publicly available via PANGAEA (PDI-21505; https://doi.pangaea.de/10.1594/PANGAEA.909101). Additional data related to this study are available from the corresponding author on request. Publicly available data used in this study are described below. Carbonate chemistry measurements made within the SBB were collected seasonally by the California Cooperative Oceanic Fisheries Investigations time-series (CalCOFI; http://calcofi.org/) and during several NOAA West Coast Ocean Acidification Cruises (WCOA; https://www.nodc.noaa.gov/ocads/oceans/Coastal/WCOA.html). Observational data from the Hawaii Ocean Time-series

program (HOT; http://hahana.soest.hawaii.edu/hot/) were also used. Shore Station Data (salinity; https://shorestations.ucsd.edu/shore-stations-data/) were used for carbonate system calculations.

References

51. Bemis, B. E., Spero, H. J. & Thunell, R. C. Using species-specific paleotemperature equations with foraminifera: a case study in the Southern California Bight. *Mar. Micropaleo.* **46**, 405–430 (2002).
52. Darling, K. F. et al. Molecular evidence for genetic mixing of Arctic and Antarctic subpolar populations of planktonic foraminifers. *Nature* **405**, 43–47 (2000).
53. Sautter, L. R. & Thunell, R. C. Seasonal variability in the $\delta^{18}O$ and $\delta^{13}C$ of planktonic foraminifera from an upwelling environment: sediment trap results from the San Pedro Basin, Southern California Bight. *Paleoceanography* **6**, 307–334 (1991).
54. Marshall, B. J. et al. Morphometric and stable isotopic differentiation of *Orbulina universa* morphotypes from the Cariaco Basin, Venezuela. *Mar. Micropaleo* **120**, 46–64 (2015).
55. Moore, W. S. Radium isotope measurements using germanium detectors. *Nucl. Instrum. Methods Phys. Res.* **223**, 407–411 (1984).
56. Bruland, K. W. *Pb-210 Geochronology in the Coastal Marine Environment.* PhD thesis, Univ. California (1974).
57. Koide, M., Soutar, A. & Goldberg, E. D. Marine geochronology with ^{210}Pb. *Earth Planet. Sci. Lett.* **14**, 422–446 (1972).
58. Krishnaswami, S., Lai, D., Amin, S. & Soutar, A. Geochronological studies in Santa Barbara Basin: ^{55}Fe as a unique tracer for particulate settling. *Limnol. Oceanogr.* **18**, 763–770 (1973).
59. Carter, M. W. & Moghissi, A. A. Three decades of nuclear testing. *Health Phys.* **33**, 55–71 (1977).
60. Ritchie, J. C. & McHenry, J. R. Application of radioactive fallout Cesium-137 for measuring soil erosion and sediment accumulations rates and patterns: a review. *J. Environ. Qual.* **19**, 215–233 (1989).
61. Shchepetkin, A. F. & McWilliams, J. C. The regional oceanic modeling system (ROMS): a split-explicit, free-surface, topography-following-coordinate oceanic model. *Ocean Model.* **9**, 347–404 (2005).
62. Gruber, N. et al. Eddy-resolving simulation of plankton ecosystem dynamics in the California Current System. *Deep Sea Res. Pt I* **53**, 1483–1516 (2006).
63. Gruber, N. et al. Rapid progression of ocean acidification in the California Current System. *Science* **337**, 220–223 (2012).
64. Hauri, C. et al. Spatiotemporal variability and long-term trends of ocean acidification in the California Current System. *Biogeosciences* **10**, 193–216 (2013).
65. Dee, D. P. et al. The ERA-Interim reanalysis: configuration and performance of the data assimilation system.*Q. J. R. Meteorol. Soc.* **137**, 553–597 (2011).
66. Graven, H. D., Gruber, N., Key, R., Khatiwala, S. & Giraud, X. Changing controls on oceanic radiocarbon: new insights on shallow-to-deep ocean exchange and anthropogenic CO_2 uptake. *J. Geophys. Res.* https://doi.org/10.1029/2012JC008074 (2012).
67. Leinweber, A. & Gruber, N. Variability and trends of ocean acidification in the Southern California current system: a timeseries from Santa Monica Bay. *J. Geophys. Res.* **118**, 3622–3633 (2013).
68. Lee, K., Kim, T.-W., Byrne, R. H. & Liu, Y.-M. The universal ratio of boron to chlorinity for the North Pacific and North Atlantic Oceans. *Geochim. Cosmochim. Acta* **74**, 1801–1811 (2010).
69. Zeebe, R. E. & Wolf-Gladrow, D. A. (eds) in *CO_2 in Seawater: Equilibrium, Kinetics, Isotopes* Vol. 65, 346 (Elsevier, 2001).

Acknowledgements

We dedicate this manuscript to co-author Robert C. Thunell, a wonderful colleague, friend and mentor, who lost his battle to cancer on 30 July 2018. This research was supported in part by a National Science Foundation grant to R.C.T. (1631977) and the Johanna M. Resig Fellowship granted to E.B.O. by the Cushman Foundation. R.A.F. was supported by the NOAA Ocean Acidification Program (PMEL contribution number 4546). N.G. acknowledges the support of ETH Zürich and of the Swiss National Foundation through the XEBUS project. We thank D. Burdige from Old Dominion University for collecting the box core used in this study; E. Tappa for his assistance with IRMS analyses and sediment trap recovery and deployments in the SBB; and N. Umling, whose review and scientific discourse greatly improved this manuscript.

Author contributions

E.B.O. and R.C.T. conceived the study and wrote the initial draft of the paper. E.B.O. designed and performed the analyses and has led the revision of the paper. N.G. and R.A.F. provided model and in situ data and contributed sustantially to the discussion and interpretation of the results and writing of the paper. C.R.B.-N. conducted radiochemistry analyses, produced an age model for the core and contributed to the interpretation and writing of the paper.

Competing interests

The authors declare no competing interests.

Additional information

Extended data is available for this paper at https://doi.org/10.1038/s41561-019-0499-z.

Correspondence and requests for materials should be addressed to E.B.O.

Peer review information Primary Handling Editor: James Super.

Reprints and permissions information is available at www.nature.com/reprints.

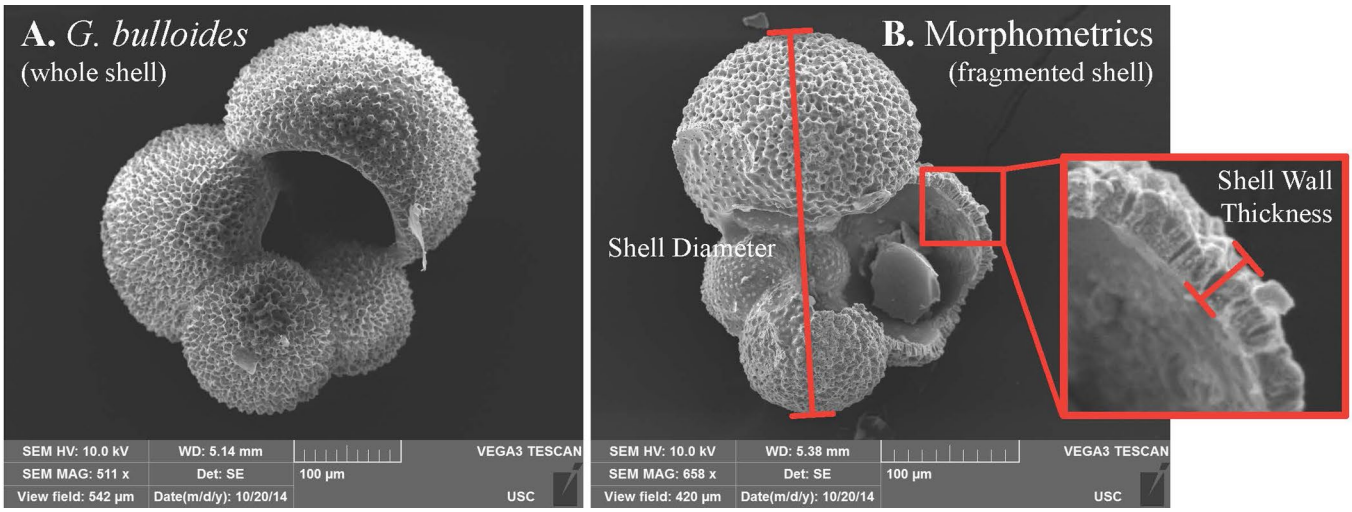

Extended Data Fig. 1 | Scanning Electron Microscope images of the study species, *G. bulloides*. B. G. bulloides shell with its final chamber broken showing a cross-sectional view of the shell wall, the key morphometric used in this study to estimate [CO_3^{2-}]. Shell wall thickness is indirectly estimated by measuring area normalized shell weight (ANSW: shell weight (μg) / 2-D surface area (μm2).

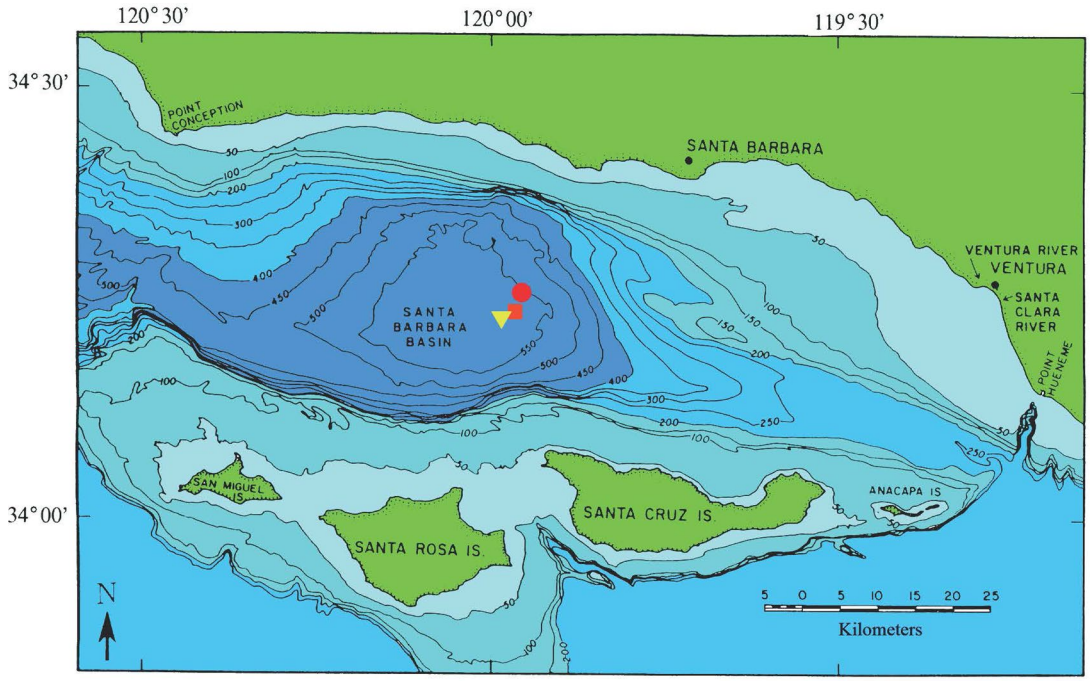

Extended Data Fig. 2 | Bathymetric map of the Santa Barbara Basin. The location of the box-core (red circle) used for the down-core reconstruction as well as the sediment trap (yellow triangle) and hydrographic sampling location (Plumes and Blooms Project Station 4; orange square) used in the calibration portion of the study[29].

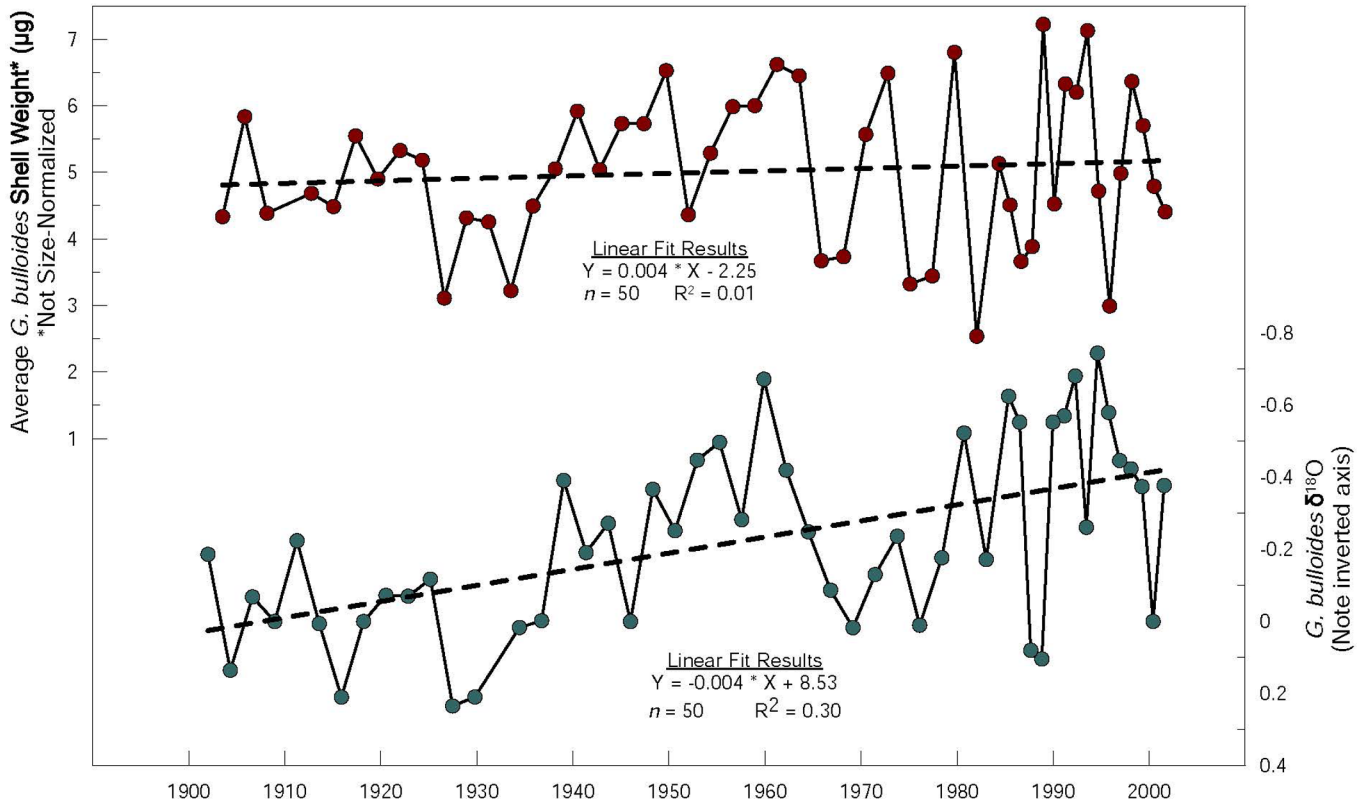

Extended Data Fig. 3 | Down core trends in G. bulloides weight (not size-normalized) and δ18O. The increasing shell weight over the down core record coincides with a decline in δ18O (note inverted axis), which represents an increase in temperature. This comparison provides a visualization of the importance of using size-normalized shell weights to estimate changes in calcification and shell thickness. Results from this study show that while overall shell weight and shell size are increasing as a result of warming temperatures, shell thickness is declining as a result of reduced [CO32-].

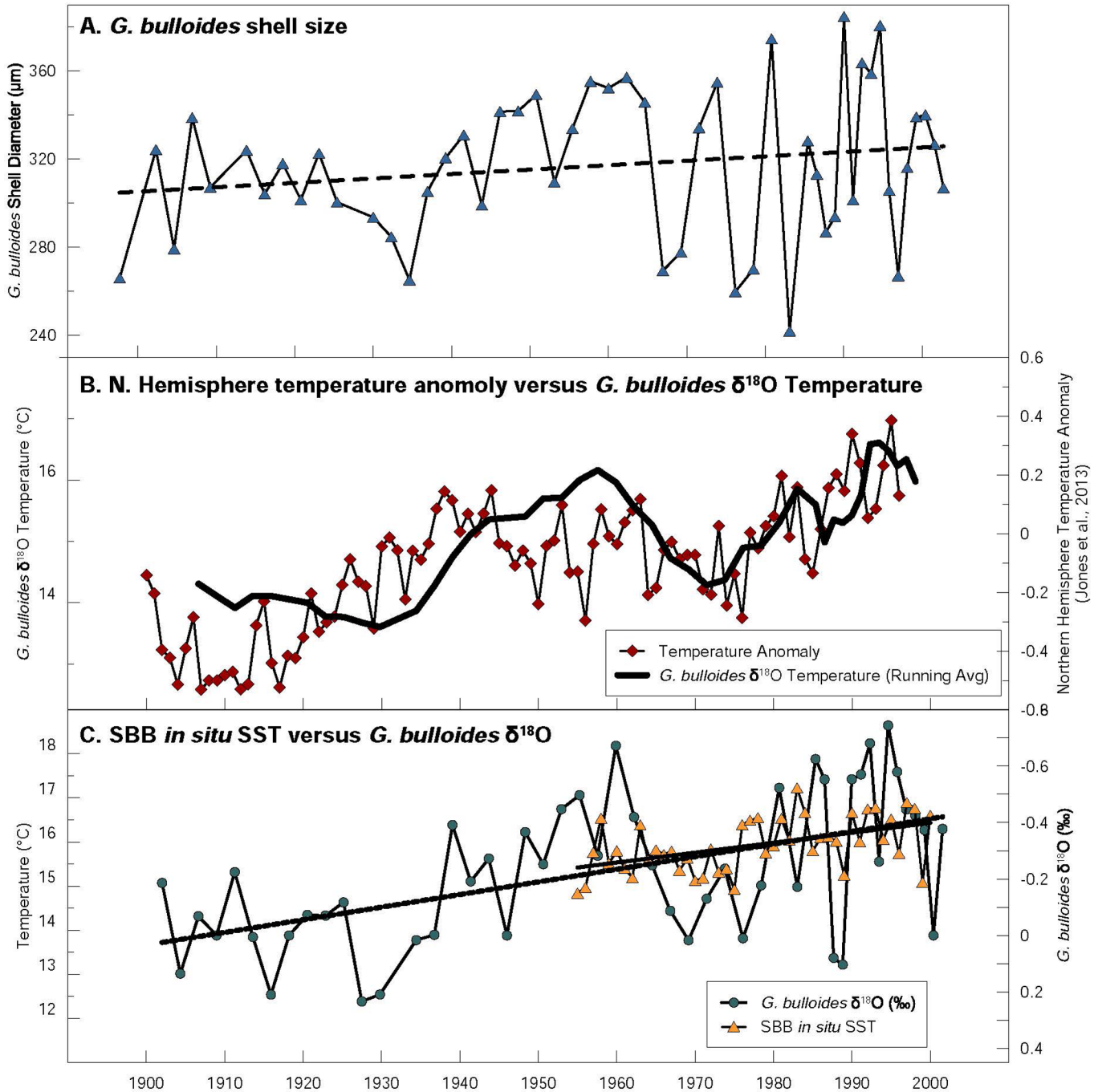

Extended Data Fig. 4 | The long-term shift in G. bulloides shell diameter increases in concert with warming sea surface temperatures. B. We compare the relative changes that are recorded G. bulloides δ18O to a Northern Hemisphere Temperature anomaly for the 1900–2000 period and see a good agreement between temperature trends recorded in these records (Jones et al., 2013). C. We also compared G. bulloides δ18O to in situ sea surface temperature (SST) measurements made in the Santa Barbara Basin (SBB; 1955-Present; Shore Stations Program) and see an excellent agreements between sea surface temperature and the δ18O recorded in our G. bulloides shells.

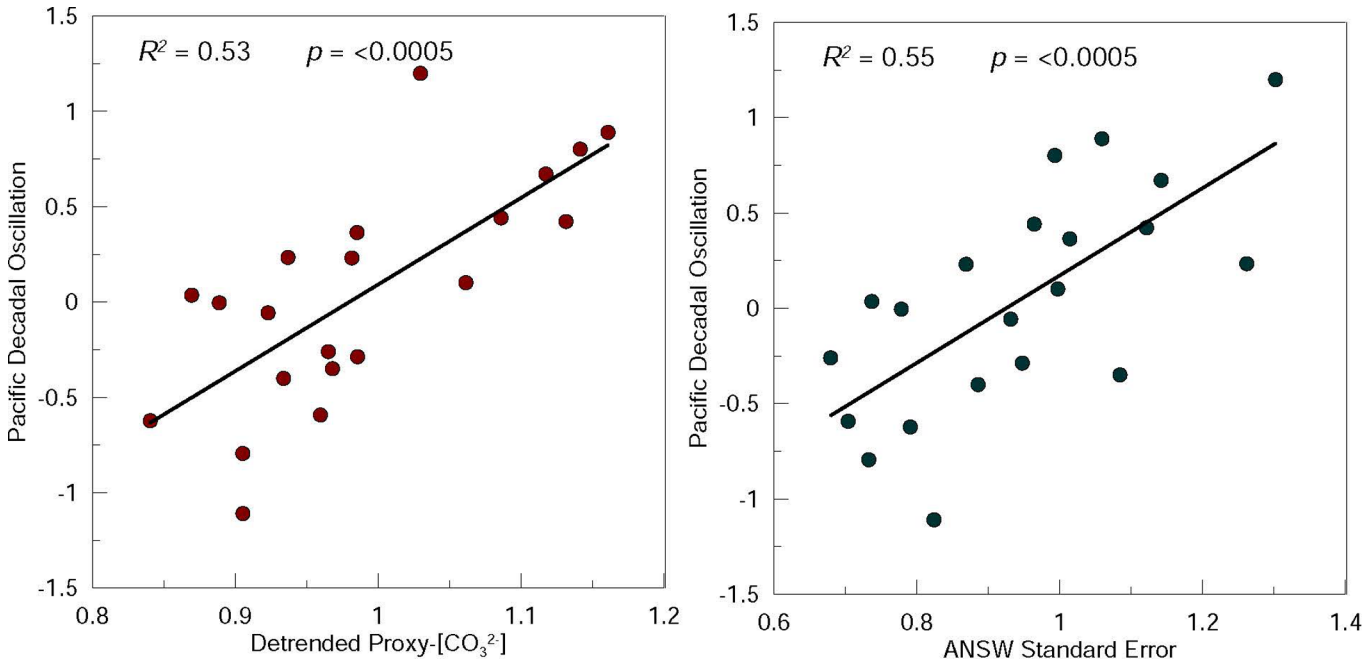

Extended Data Fig. 5 | Time-series correlations between Pacific Decadal Oscillation Index and the detrended proxy-[CO3=] and ANSW sample standard error. Corresponding values were compared at 5-year time steps due to difference in time resolution across records. An independent t-test was conducted to compare both detrended proxy-[CO3=] and area-normalized shell weight standard area (a measure of sample variability) to the Pacific Decadal Oscillation Index. Highly significant correlation coefficients exist between PDO and the respective variables p<0.005) and the results of a paired t-tests for both records are highly significant (p<0.005), further confirming significance of the relationships.

Science of the Total Environment xxx (xxxx) xxx

Contents lists available at ScienceDirect

Science of the Total Environment

journal homepage: www.elsevier.com/locate/scitotenv

Exoskeleton dissolution with mechanoreceptor damage in larval Dungeness crab related to severity of present-day ocean acidification vertical gradients

Nina Bednaršek [a,*], Richard A. Feely [b], Marcus W. Beck [c], Simone R. Alin [b], Samantha A. Siedlecki [d], Piero Calosi [e], Emily L. Norton [f], Casey Saenger [f], Jasna Štrus [g], Dana Greeley [b], Nikolay P. Nezlin [a], Miranda Roethler [a], John I. Spicer [h]

[a] Southern California Coastal Water Research Project, Costa Mesa, CA 92626, USA
[b] NOAA Pacific Marine Environmental Laboratory, 7600 Sand Point Way NE, Seattle, WA 98115, USA
[c] Tampa Bay Estuary Program, 263 13th Ave S, St. Petersburg, FL, 33701, USA
[d] Department of Marine Sciences, University of Connecticut, Groton, CT 06340, USA
[e] Département de Biologie, Chimie et Géographie, Université du Québec à Rimouski, 300 Allée des Ursulines, Rimouski, QC G5L 3A1, Canada
[f] Joint Institute for the Study of the Atmosphere and Ocean, University of Washington, Seattle, WA 98195, USA
[g] Department of Biology, Biotechnical Faculty, University of Ljubljana, Ljubljana, 1000, Slovenia
[h] University of Plymouth, School of Biological and Marine Sciences, Plymouth PL4 8AA, UK

HIGHLIGHTS

- Coastal habitats with the steepest ocean acidification gradients are most detrimental for larval Dungeness crabs.
- Severe carapace dissolution was observed in larval Dungeness crabs along the US west coast.
- Mechanoreceptors with important sensory and behavioral functions were destabilized.
- Dissolution is negatively related to the growth, demonstrating energetic trade-offs.
- 10% dissolution increase over the last two decades estimated due to atmospheric CO_2.

GRAPHICAL ABSTRACT

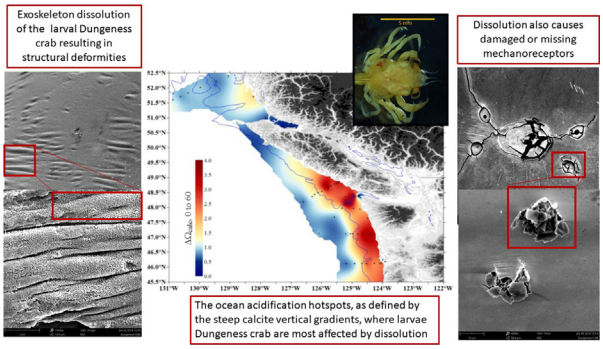

ARTICLE INFO

Article history:
Received 8 November 2019
Received in revised form 4 January 2020
Accepted 7 January 2020
Available online xxxx

Editor: Henner Hollert

Keywords:
Dungeness crab
Larval sensitivity

ABSTRACT

Ocean acidification (OA) along the US West Coast is intensifying faster than observed in the global ocean. This is particularly true in nearshore regions (<200 m) that experience a lower buffering capacity while at the same time providing important habitats for ecologically and economically significant species. While the literature on the effects of OA from laboratory experiments is voluminous, there is little understanding of present-day OA *in-situ* effects on marine life. Dungeness crab *(Metacarcinus magister)* is perennially one of the most valuable commercial and recreational fisheries. We focused on establishing OA-related vulnerability of larval crustacean based on mineralogical and elemental carapace to external and internal carapace dissolution by using a combination of different methods ranging from scanning electron microscopy, energy dispersive X-ray spectroscopy, elemental mapping and X-ray diffraction. By integrating carapace features with the chemical observations and biogeochemical model hindcast, we identify the occurrence of external carapace dissolution related to the steepest Ω calcite

* Corresponding author.
E-mail address: ninab@sccwrp.org (N. Bednaršek).

https://doi.org/10.1016/j.scitotenv.2020.136610
0048-9697/© 2020 Elsevier B.V. All rights reserved.

Global climate change
Ocean acidification
Exoskeleton structure
Dissolution
Mechanoreceptor damage

gradients ($\Delta\Omega_{cal,60}$) in the water column. Dissolution features are observed across the carapace, pereopods (legs), and around the calcified areas surrounding neuritic canals of mechanoreceptors. The carapace dissolution is the most extensive in the coastal habitats under prolonged (1-month) long exposure, as demonstrated by the use of the model hindcast. Such dissolution has a potential to destabilize mechanoreceptors with important sensory and behavioral functions, a pathway of sensitivity to OA. Carapace dissolution is negatively related to crab larval width, demonstrating a basis for energetic trade-offs. Using a retrospective prediction from a regression models, we estimate an 8.3% increase in external carapace dissolution over the last two decades and identified a set of affected OA-related sublethal pathways to inform future risk assessment studies of Dungeness crabs.

© 2020 Elsevier B.V. All rights reserved.

1. Introduction

Since the pre-industrial era, anthropogenic CO_2 uptake along the US West Coast have resulted in rapid intensification OA rate on a global scale (Chavez et al., 2017; Feely et al., 2016), resulting in lower carbonate conditions compared to the pre-industrial times. This is because of the low regional buffering capacity, which contributes to low pH and carbonate mineral saturation states for both aragonite (Ω_{ara}) and calcite (Ω_{cal}) (Feely et al., 2018). These changes in carbonate chemistry have resulted in substantially reduced habitat suitability for marine calcifiers (Bednaršek et al., 2014; Somero et al., 2015). These findings are supported by the field and synthesis work along the North American Pacific demonstrating that calcifying invertebrates will be the ones most impacted by progressive OA (Bednaršek et al., 2017; Busch and McElhany, 2016). Apart from evidence of OA impacts on pteropods and other calcifiers caused by the low Ω_{ara} conditions in upwelling systems (Bednaršek et al., 2014, 2017) and around CO_2 vent seeps and sites (Manno et al., 2019; Tunnicliffe et al., 2009), there is limited understanding of present-day OA effects on marine life *in situ*. That is especially relevant for the crustaceans since they were considered less sensitive to OA parameters (like pCO_2 or pH) after studies demonstrated their capacity to abate initial hypercapnia and to buffer extracellular acid-base disturbances (Melzner et al., 2009; Pane and Barry, 2007) with limited or no change in aerobic metabolism (Paganini et al., 2014). However, restoring internal pH to sustain physiological and biogeochemical processes (Somero, 1986), typically requires activation of buffering, which is energetically expensive process (Cameron, 1985; Michaelidis et al., 2005). Recent experimental findings have demonstrated increased sensitivity to OA-related stressors in crustaceans, especially in the early life stages that can be regarded as a potential bottleneck for the population level responses (Schiffer et al., 2014; Small et al., 2015). Regardless of the habitats that different species inhabit, the studies investigating OA effect on larval stages reported lower growth and decreased survival of blue crab (Giltz and Taylor, 2017), delayed metamorphosis in the stone crab (Gravinese et al., 2018), changes in exoskeleton composition (Page et al., 2016) and decreased metabolisms in Tanner crabs (Long et al., 2016) and increased energetic costs in the porcelain crab (Carter et al., 2013), while the pre-larval of the Dungeness crab showed reduced survival and slower progression through the development (Miller et al., 2016). With annual revenues up to $220 million (Hodgson et al., 2018; Pacific States Marine Fisheries Commission, 2019), the Dungeness crab (*Metacarcinus magister*) is one of the most valuable and recreational fisheries in the US coastal waters. Terminal stage of pelagic Dungeness crab larvae (megalopae) undergoes long distance transport along the north Pacific coast of North America before settling in suitable benthic settlement site (Shanks, 1995; Sinclair, 1988). Given their diel vertical migration extends down to 60 m depth (Hobbs et al., 1992), megalopae encounter steep vertical pH, Ω_{cal} gradients in coastal habitats; however, the duration and magnitude of their exposure to these conditions remains largely unknown despite the exposure history notably impacting organismal responses (*sensu* Bednaršek et al. (2017).

To start addressing potential OA vulnerability of the pelagic Dungeness larvae *in situ*, their spatial distribution must be paired with *in situ* exposure history (as defined in Bednaršek et al., 2017), understanding of their physiological susceptibility and their structural and mineralogical features. In regards to the later, surprisingly little is known about these features that can predispose an individual to extensive exoskeleton dissolution if the conditions in the external environment are conducive for it. In addition, for detecting environmental clues, the decapod exoskeleton contains elongated hair-like structures called setae, which are important chemo- and mechanoreceptors involved in sensory and behavioral responses. While the lipoproteic epicuticle-covered exoskeleton consists of two cuticular mineral carbonate layers (Chen et al., 2008) (*i.e.*, the outer exocuticle and the inner endocuticle) in the Dungeness crab adults such structure or its composition is completely unknown for the larvae.

This interdisciplinary study integrates physical, geochemical, biological, and modelling components across the individual and population-level parameters. Identification of the carapace crystalline mineralogical and elemental composition provided an understanding behind the extensive exoskeleton dissolution and mechanoreceptor damage. The latter was linked with the chemical observations made along the North American West Coast to identify the drivers and OA hotspots of *in situ* megalopae vulnerability. The biogeochemical model hindcast was used to determine the impact of *in situ* exposure history in the coastal habitats.

2. Materials and methods

2.1. Carbonate chemistry, sampling and analyses

For the purpose of this study, the NOAA West Coast Ocean Acidification (WCOA) cruise in May–June 2016 sampled conductivity, temperature, depth, and oxygen. Data on the conductivity, temperature, and pressure of seawater (CTD) were collected along cross-shelf transects, accompanied by biological stations with vertical sections of temperature (T), salinity, nutrients, oxygen, chlorophyll-a (chl-a), dissolved inorganic carbon (DIC), total alkalinity (TA), spectrophotometric pH (measured at 25 °C and corrected to *in situ* temperatures, and expressed on the total pH scale, subsequently expressed pH_T). pCO_2 and calcite saturation state (Ω_{cal}) were calculated using CO2SYS as described by Feely et al. (2016) and Bednaršek et al. (2012). Larvae were collected using Neuston and Bongo nets with a mesh size of 333 μm, which were deployed in an oblique manner at 10 stations during the night in the upper surface waters, an area that encompasses the nocturnal vertical habitat of larval Dungeness crabs of the upper 60 m (Hobbs et al., 1992; Morgan, 1989), with the following environmental parameters along the vertical habitat (Table S1). The duration of tows was 15–20 min. Megalopae were identified and then stored in 100% non-denatured ethanol, and also flash-frozen at −80 °C for later comparison of two different preservation methods.

2.2. Using SEM methods to detect and evaluate carapace dissolution

Megalopae carapaces were investigated using a combination of different methods: 1) scanning electron microscopy (SEM; Hitachi Phenom, USA) to determine potential structural changes on the cuticular

surface; 2) energy dispersive X-ray spectroscopy (EDXS at the University of Washington) for mineralogical composition; 3) elemental mapping; and X-ray diffraction (University of Washington and Max Planck Institute) for elemental content across mostly lipoproteic carapace (Fig. S1, Fig. 1). Here, we define exoskeleton as the cuticle covering the dorsal part of the carapace of the larval crab, and five pereopods, with chelae. The carapace epicuticle, which otherwise overlies the crystalline layer and makes dissolution observations impossible, was removed from each megalopa prior to analysis. This was accomplished using sodium hypochlorite, which efficiently removes the epicuticle but does not damage the crystalline layers underneath, even at high concentrations (Bednaršek et al., 2012). On the samples with no hypochlorite treatment, the epicuticle covered the crystalline layer so no investigation of dissolution was possible. Therefore, we tested different concentrations and duration of hypochlorite treatment on the individuals from the same station to ensure that we fully removed the epicuticle, without triggering dissolution of the calcite crystalline layers beneath it. The combination of 1 and 3% sodium hypochlorite with 15, 30, and 120 min treatments only partially removed the epicuticle, while 6% hypochlorite treatments for 4 and 6 h were effective in epicuticle removal, without inducing additional dissolution at the longer duration.

To determine the treatment does not induce any damage, we have tested the individuals from the same stations with different combination of treatments. We assumed the similarity of exposure history of individuals within the same stations (see modelling section). The results of no difference in dissolution under the different combination of concentration/duration of treatment combination was a confirmation that the treatment did not induce any additional damage, and thus did not confound our field observations.

We determined 6% hypochlorite for 3–4 h to be an efficient and effective treatment, similar to the treatment previously described for the removal of the periostracum in pteropods (Bednaršek et al., 2012). After soaking in sodium hypochlorite, samples were rinsed several times in Millipore water to remove any organic matter remaining on the surface of the exoskeleton. It is important to note that when examining the presence of setae within the neuritic canals, we did not use any treatment in order to avoid any methodological artifacts. When examining the internal area of the cuticle, we avoided examining the proximity of the gills given that dissolution could be impacted by the processes around. To quantify the dissolution of internal carapace cuticle, the pereopods and soft tissue of larvae were gently removed from the rest of the body and washed in Millipore water to remove any remaining tissue or organics before treatment with sodium hypochlorite. Each of the five

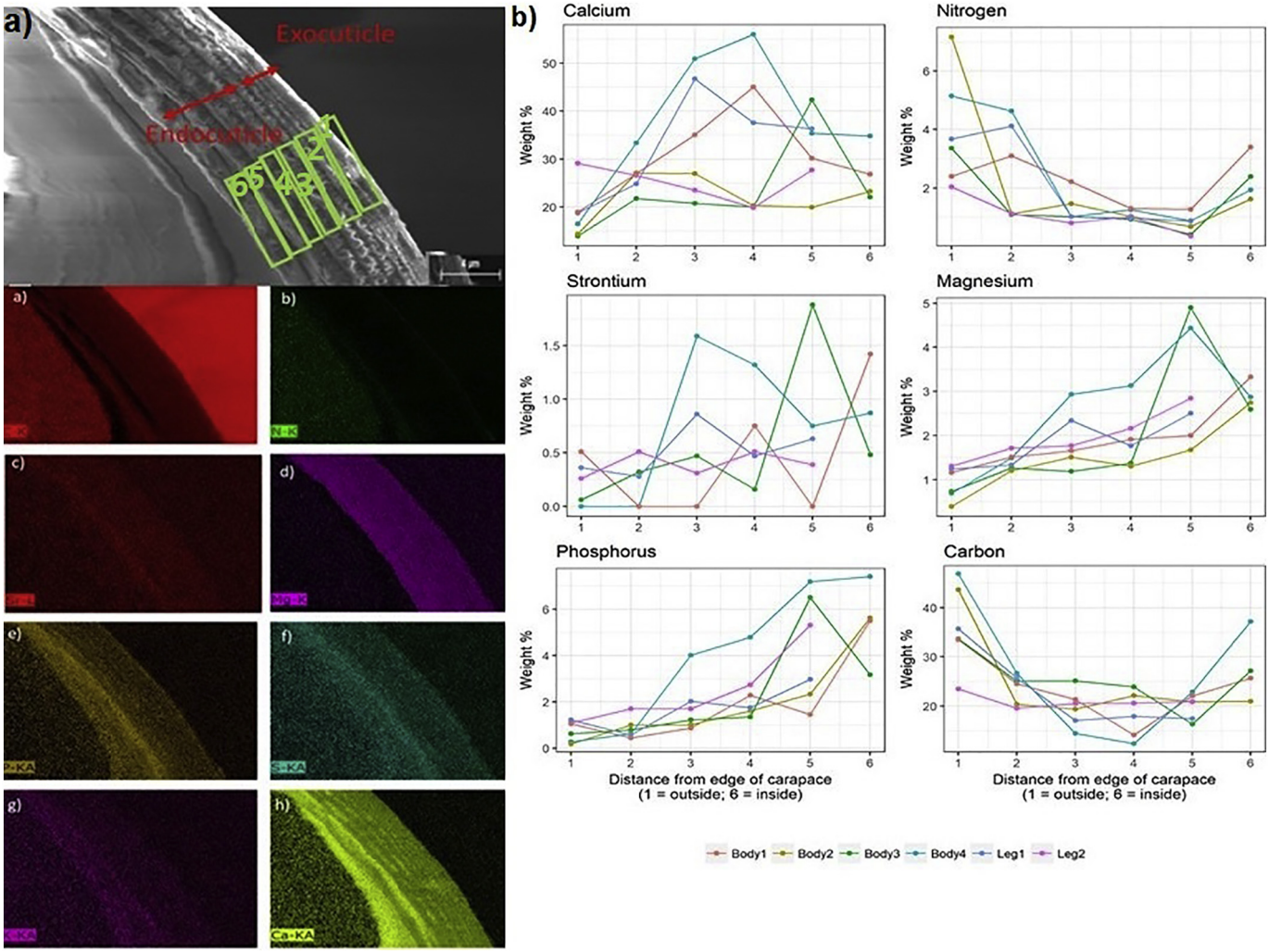

Fig. 1. The cross sections of the Dungeness crab megalopae. Left panel (a): cross section of carapace (with increasing numbers describing the transition from the thinner *exo*- (1) to thicker *endo*-cuticle (6). Right panel (b): distribution of various elements (C-carbon-a; N-nitrogen-b; Sr^{2+}- strontium-c; Mg^{2+}- magnesium-d; P-phosphor-e; S-sulphur-f; K-potassium-g, Ca^{2+}-calcium-h). The more intense colors depict higher elemental concentration. Spectrum and % content of selected elements in either carapace or pereopod exoskeleton (*a*). The numbers in (*a*) coincide with the numbers in (*b*) that indicate the position within the carapace.

pereopod cuticle was examined across the proximal and distal ends, with particular focus on chelae (Fig. S2). SEM was used to evaluate the extent and severity of dissolution. We focused on three distinct features: ridging structures, dissolution around setae, and exposed calcite crystals (Fig. S2, S3).

For estimating the various body parameter change (in mm) of larvae across various vertical OA gradients, we have measured carapace length (CL), total length from rostrum to telson (TL), length from rostrum to dorsal carapace spine (R-DCS), and carapace width (CW). The CW is the most commonly used parameter by various US federal agencies along the US West Coast to regulate crab management catch efforts (Davis et al., 2017). Here, we assume that all the larvae were released at the same time to allow for body parameter comparisons across different stations. Using the methodology to characterize the megalopae stages by González-Gordillo et al. (2004), we determined that all megalopae were in the intermolt stage, except for those from Station 115, which were transitioning into the premolt stage. We excluded the results of the internal dissolution observations from this station in case promoting process changed any features on the internal side that could bias accurate dissolution assessment.

2.3. Semi-quantitative dissolution assessment

Altogether, we analyzed 50 individuals from 10 environmental stations across OA-related vertical gradients of varying strength. We used 3–5 individuals per station to determine dissolution extent of the external side of carapace cuticle, as well as the cuticle of the pereopods. We used an additional 2–3 individuals per station to analyze the internal side of the cuticle. Approximately 10–20 SEM images were produced per individual on the external and internal sides, with the images being manually examined to detect any signs of dissolution. For crystal exposure characterization, the same categorization of dissolution conditions as previously described in pteropods was used (Bednaršek et al., 2012). We identified three major features of exoskeleton dissolution and developed a categorization scheme for all three features, showing them in their intact forms (Stage 0, Fig. S2) and progressively altered forms (Stage 1 and 2; Fig. S1; Table S2). These features differentiated damaged surfaces from the intact surfaces (Table S2). The cuticular surface of the carapace and the pereopods under high Ω_{cal} *in situ* conditions had a smooth, sleek appearance (Fig. S2; Stage 0). At greater magnification, individual calcite crystals were visible in these areas (Fig. S2). Signs of dissolution tended to be more prevalent and more severe on the surface immediately surrounding setae pores. Consequently, areas around the setae were considered separately from the rest of the exoskeleton. From these observations, a semi-quantitative scoring metric was developed based on previous work on pteropods and used to score the remainder of the samples. For each sample, the three separate features (presence and depth of ridge structures, exposure of individual calcite crystals, and the prevalence of dissolution features around setae pores) were each assigned a score. The features were scored on a scale of 0 to 1 based on the severity of dissolution: intact exoskeleton with no dissolution received a score of 0; moderate dissolution received a score of 0.5; and substantial dissolution of all examined features was scored 1 (Figs. S1–S3). Since the crab exoskeleton of the carapace and pereopod differ in their chemical composition, these three areas were assigned separate scores. Because of the surface analyses required separately for the external and internal dissolution, both types of analyses could not be conducted on the same individual. All three features displayed similar trends, so the scores were averaged to unitless 'relative dissolution', describing internal and external dissolution. Observation of setae presence/absence was included in the exoskeleton observation under SEM on intact specimen before any preparation treatments were conducted to eliminate the possibility of preparation steps affecting setae presence or outrooting them from the carapace.

2.4. Mineralogical analyses

The mineralogy of selected megalopae was characterized using X-ray diffraction (D8 Discover 2D; University of Washington, Seattle). Prior to analysis, carapaces from five megalopae at each site were coarsely crushed and treated for 10 min using a dilute (3%) sodium hypochlorite solution to minimize interference from organic matter but without compromising mineralized structures. Samples were dried completely and then ground to a fine homogenous powder representing the aggregate of the five individuals from each location. Resulting diffractograms were compared to a catalog of mineral-specific patterns to constrain the primary mineralogy of each sample.

2.5. Elemental analyses

We used energy-dispersive X-ray spectroscopy (EDXS) to estimate elemental composition of the carapace and pereopod cross-sections ($N = 7$) from samples across different natural OA vertical gradients over spatial scales. For elemental analyses, we have not removed the epicuticle from the samples. These gradients analyses were conducted at Max Planck Institute for Marine Microbiology in Bremen, Germany. Prior to analyses, we dehydrated samples using 100% ethanol and dried them in a critical point dryer. We prepared the sections by fracturing different carapace regions which was followed by the EDXS investigations (Fig. 1).

2.6. Statistical analyses

Biological measurements from Dungeness megalopae collected at 10 stations along the North American Pacific Coast (Fig. 2) were paired with synoptic environmental data from CTD profiles. Environmental data were summarized as depth-integrated averages from the surface to the maximum depth of each CTD profile to characterize the exposure conditions in the upper water column. In addition, $\Delta\Omega_{cal,60}$ was estimated as the difference from the observed measurement at each depth bin with that of the surface. This measurement characterized the relative Ω_{cal} gradients with increasing depth and accounted for differences in the relative magnitudes of Ω_{cal} between stations. Chlorophyll-a observations were highly skewed and so were log-transformed prior to analysis.

Biological responses included dissolution, body parameter, and abundance with various environmental vertical gradients to identify significant associations using generalized linear models. For comparison of the biological data to environmental conditions, each depth bin for the depth-integrated values was evaluated to identify at which depth associations between biological response and selected environmental variables were strongest. In addition, carapace dissolution was compared to body parameters to characterize potential linkage between the physiological parameters, growth, and population-level effects (abundance). Comparisons of biological measures to each other were also accomplished with generalized linear models.

Gaussian distributions were assumed for all response variable models, excluding presence/absence, which was modeled using a binomial logistic response curve. Models and individual parameters were considered significant at $\alpha = 0.05$. All models had $N = 10$ except presence/absence models with $N = 24$, which included additional stations where tows were conducted but no crabs were found. Finally, all variables were evaluated together to identify pairwise associations using Pearson correlation analysis and redundancy analysis (RDA) to characterize how the biological response measures were jointly explained by the environmental variables. For the latter analysis, all input data were standardized to range from 0 to 1 to account for differences in scale between variables. The *vegan* package for the R statistical programming language was used for standardization and RDA (Oksanen et al., 2019; R Core Team, 2019).

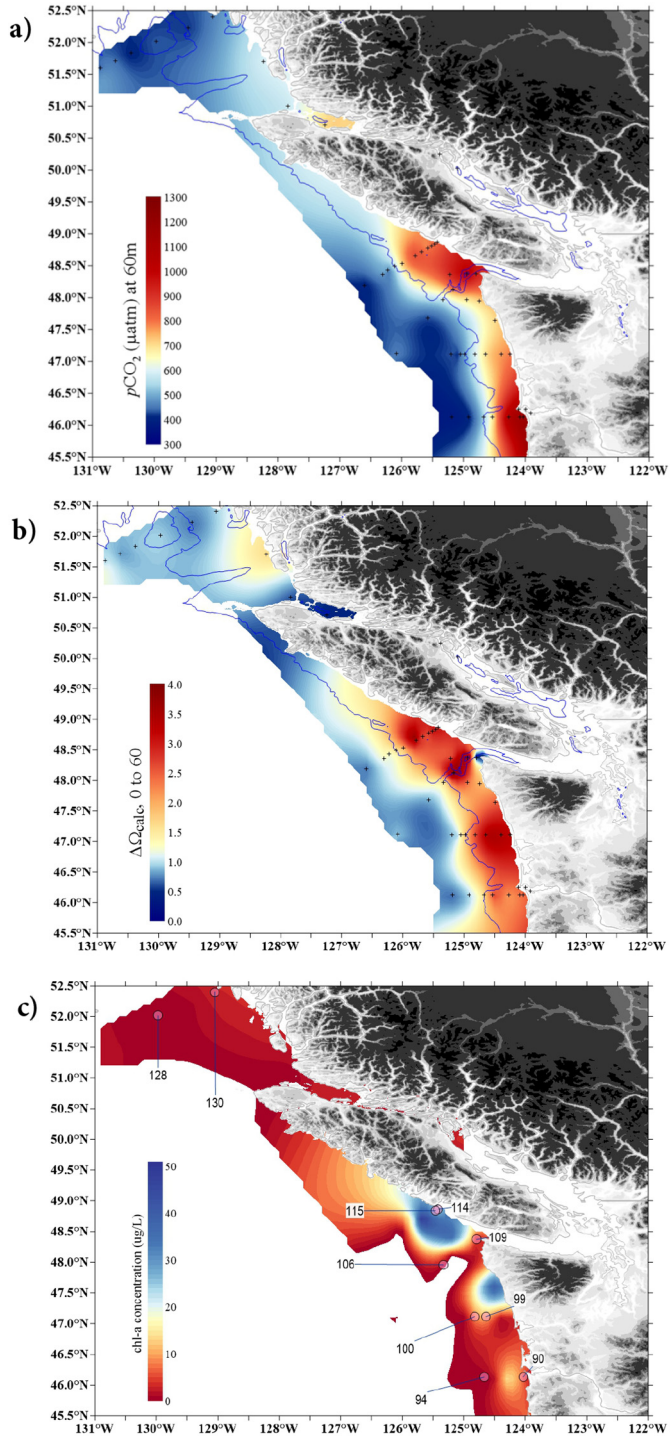

Fig. 2. Interpolated $pCO_{2,60}$ (*a*), $\Delta\Omega_{cal,60}$ (*b*) and chlorophyll (*c*) conditions in the onshore and offshore habitats along the US West Coast in June 2016. pCO_2 reflects the conditions at 60 m depth and $\Delta\Omega_{cal,60}$ indicates the difference between the surface and 60 m depth. *c*) Chlorophyll distribution and concentration (chl-a; µg/L) demonstrate an order of magnitude difference between the regional nearshore and offshore region. The numbers indicate the stations at which the crabs were collected.

For selected predictors, additional models were developed to evaluate the additive effects of two predictors on dissolution. Backward model selection was used to identify the most parsimonious model by sequentially dropping individual predictors and comparing Akaike Information Criterion values (AIC) (Akaike, 1973; Fox and Weisberg, 2011). This allowed us to determine if there was any additional power in combining predictors to explain dissolution, or consequently, if dissolution could be sufficiently explained using only one predictor. For example, the ability of both Ω_{cal} and chlorophyll to explain dissolution were evaluated to better understand the relative effects of both.

2.7. J-SCOPE model outputs of the larval exposure history prior to sampling

The Joint Institute for the Study of the Atmosphere and Ocean (JISAO)'s Seasonal Coastal Ocean Prediction of the Ecosystem (J-SCOPE, http://www.nanoos.org/products/j-scope/) features dynamical downscaling of regional ocean conditions in Washington and Oregon waters (Siedlecki et al., 2016). Model performance and predictability examined for sea surface temperature (SST), bottom temperature, bottom O_2, pH, and Ω_{ara} through model hindcast, reforecast, and forecast comparisons with observations, showing significant measurable skill on seasonal timescales (Kaplan et al., 2016; Siedlecki et al., 2016; Norton et al., *in revision*). Megalopae exposure histories were simulated by releasing 100 representative particles, with vertical migration behavior over 60 m inserted into the predicted circulation field at each of the *in situ* sampling locations and times, and then tracking them backward in time for 30 d following methods described for pteropods in Bednaršek et al., 2017, and for megalopae in Norton et al., *in revision*. The vertical migration behavior was simulated using the LTRANSv2b larval transport model (North et al., 2008, 2011; Schlag and North, 2012) that has recently been implemented in the J-SCOPE system and adapted for megalopae (Norton et al., *in revision*).

3. Results

3.1. Elemental and crystalline characterization of the carapace

The compilation of our results demonstrate that the carapace is highly mineralized and precipitated into a chitin-proteinaceous matrix. XRD identify calcite as a primary polymorph in the carapace. The mineralized exoskeleton of the megalopae intermolt stages consists of the thinner exocuticle on the surface that is <2–3 µm thick, and the thicker and more compact endocuticle underneath (Fig. 1) of approximately 6–7 µm, with the combined thickness up to 10 µm. The carapace surface is extensively covered with setae that are rooted in the calcified neuritic canals each with an average of about 5 µm surface opening (Figs. S2 and S3). EDXS investigations characterized detailed elemental structure with average Ca^{2+} content of 28% in the carapace and pereopods, with much higher Ca^{2+} found within in the mid layer and the endocuticle (higher than 50%) compared to <20% found in the exocuticle (Fig. 1). The carapace endocuticle contains also a high concentration of Mg^{2+} with some areas of the carapace exceeding 5% content, categorizing it as a more soluble high-Mg calcite. In addition, the internal side contain high concentrations of phosphorus (up to 6%) and strontium (up to 2%) on the inner endocuticle (Fig. 1). The percentage of different dissolution features is similar between the carapace and the pereopods, however with much less variation in all elements between the carapace and pereopods (Fig. S1). This elemental composition indicates that other crystalline forms of carbonate could be precipitated into a chitin-proteinaceous matrix, such as an amorphous calcium carbonate (ACC) crystalline layer, but the methods used were not suitable for ACC detection. The strong presence of autofluorescence prevented more precise detection of any other crystalline forms, despite extensive use of Raman spectroscopy for this purpose. Nevertheless, such elemental structure resembles a layer of ACC with Mg^{2+}, phosphate and carbonate-rich phase, or ACC with magnesian calcite, as previously demonstrated in the edible crabs *Cancer pagurus* (Fabritius et al., 2012).

3.2. Megalopae habitat characterization with strong vertical and spatial Ω_{cal} vertical gradients

Crab megalopae were found in both outer-shelf, slope, as well as nearshore (<200 m depth) habitats, with distinctly different vertical

environmental gradients in the upper water column. Due to the upwelling of deeper, colder, CO_2-rich waters in the near-shore and coastal habitats, steep gradients in low pH and Ω_{cal} values were observed. In comparison, offshore region were characterized with more uniform vertical gradients with lower vertical difference were over the same depth interval (Fig. 2). Pronounced steep OA-related vertical habitats were observed in the upper 60 m of the water column, here represented as the difference between the surface and 60 m depth ($\Delta\Omega_{cal,60}$ or ΔpH_{60}), which is within the lower range of megalopae diel vertical migration habitat. Among all tested depths, statistical models comparing biological responses (*e.g.* exoskeleton dissolution, body parameters, abundance) with environmental conditions had the strongest associations using the 60 m vertical depth integrated value (*e.g.*, external dissolution on body parts *vs.* $\Delta\Omega_{cal}$ had the highest $R^2 = 0.821$ at 60 m). Hereafter, all environmental data are reported using the 60 m depth integrated values. Coastal conditions recorded near-saturation Ω_{cal} values down to 1.4, pH down to 7.48, and pCO_2 up to 910 uatm (Table S1; Fig. 2). There were no observations of $\Omega_{cal} < 1$ or hypoxia, with similar oxygen ranges observed in the onshore and offshore regions, while average temperature that was by about 1.3 °C warmer offshore. Food availability was an order of magnitude higher in the onshore regions compared to offshore, with the highest chl-a values recorded at 25 μg/ L (Fig. 2).

Multiple environmental parameters co-varied (Fig. 3a) as observed in the RDA plot at 60 m depth (Fig. 3b). The first two axes of the RDA explained approximately 90% of the variation among the biological and environmental parameters. The first RDA axis was characterized by a $\Delta\Omega_{cal,60}$ vertical gradient and external dissolution, with both having negative loadings along the RDA1 axis. Carapace width was negatively correlated with $\Delta\Omega_{cal,60}$, whereas external dissolution was positively correlated, suggesting that larger individuals had less dissolution and were associated with lower gradients in $\Delta\,\Omega_{cal,60}$. While OA parameters (pCO_2, pH) were all correlated as indicated by alignment with the second RDA axis, the collinearity with temperature was not significant. We found less collinearity among the environmental parameters related to the 60 m vertical gradients, such as $\Delta\Omega_{cal,60}$, $\Delta O_{2,60}$, and ΔT_{60}. Here, we focused on the mechanistic drivers that are explicitly involved in the external dissolution processes, we have examined $\Delta\Omega_{cal,60}$ in how it relates to external dissolution. Similarly, internal dissolution was negatively correlated with pCO_2 along the second axis with slightly higher loading along the RDA1, and also slightly negatively related with increased temperature. The implications of this association and how they related to model output (Fig. 7) will be explained below.

3.3. Megalopae carapace dissolution and reduced width as responses to variable OA parameters across vertical scales

Dissolution assessment on the external surface of the exocuticle and internal surface of the endocuticle of the megalopa's carapace and pereopod exoskeleton, was conducted only after confirming that sample preservation did not impact dissolution patterns, *i.e.* samples preserved in ethanol *vs.* flash frozen did not exhibit any significant difference in their dissolution features. Using a novel categorization scheme to semi-quantify dissolution features, including ridging structures, dissolved areas around neuritic canals, and exposed calcite crystals (Figs. 4, S1 and S2; Table S2), the individuals demonstrated various extents of these features present on the external side of the carapace and the pereopod exoskeleton (Fig. S2 and S3). On the carapace, the front and outer surfaces were the most affected (Figs. 4 and S3). On the pereopod exoskeleton, the thoracic segments and chelae had the most severe dissolution, while the distant parts were less affected (Fig. S3). On all of the examined individuals with external dissolution, we also found evidence for internal endocuticle dissolution, which was, on average, approximately half that observed on the external exocuticle surface.

Average dissolution on the exocuticle showed the strongest linear dependence with $\Delta\Omega_{cal,60}$ (Fig. 5; $R^2 = 0.866$, $p < .001$), demonstrating that the habitats with the steepest 60 m vertical gradients results in the most damaged organisms. Because of the topographic features, there is a spatial variability related to the occurrence of the steepest $\Delta\Omega_{cal,60}$ gradients, meaning that the lowest exoskeleton dissolution does not always correspond to the offshore gradients.

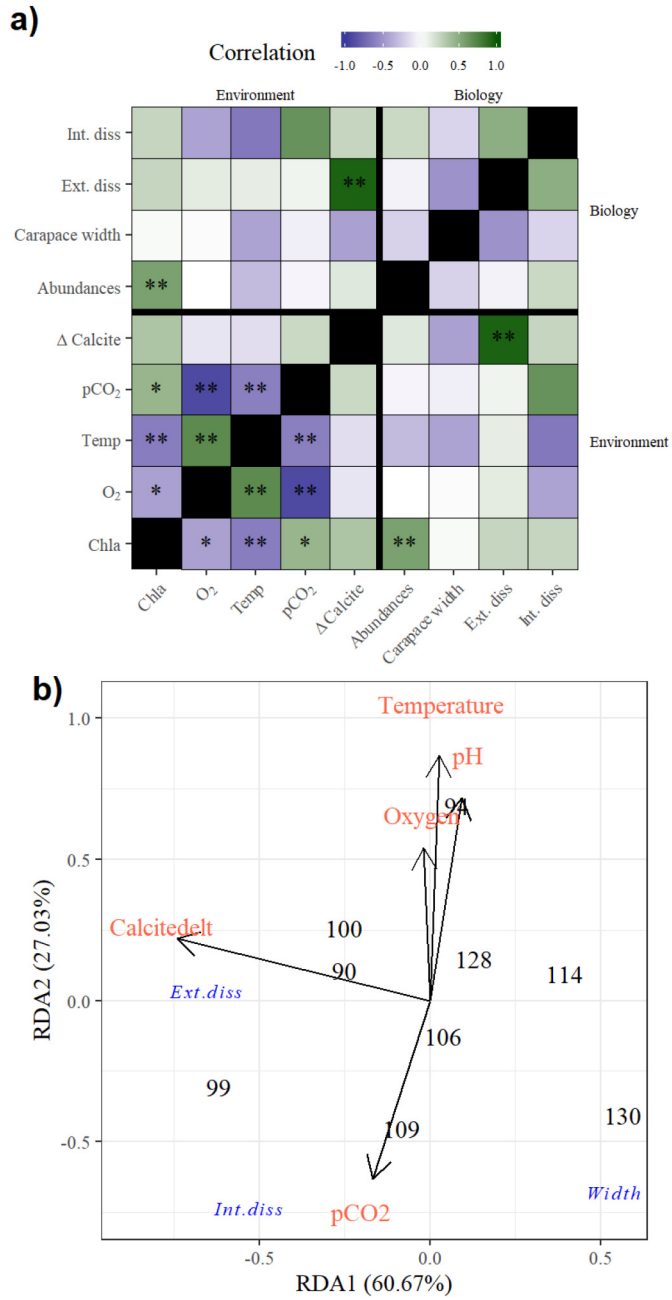

Fig. 3. Correlation matrix of environmental variables with biological endpoints for Dungeness megalopae: (*a*) Darker green values are strong positive correlations and darker purple values are strong negative correlations, while dimmer green and purple indicate weaker correlations; and *b*) Redundancy analyses (RDAs) for environmental variables used in the analyses with crab biological measurements (internal and external dissolution, carapace width). (For interpretation of the references to colour in this figure legend, the reader is referred to the web version of this article.)

The internal dissolution showed the most robust evidence, though not statistically significant, of correlation with pCO_2 values (Fig. 5; $R^2 = 0.406$, $p = .065$) and negative marginal significance with temperature ($R^2 = 0.435$, $p = .053$). The internal dissolution rapidly intensified beyond $pCO_2 > 500$ μatm (Fig. 5b), with this being a robust threshold. There was no significant correlation between internal and external dissolution (Fig. 5; $p = .18$), suggesting decoupling of the two processes.

At sites with a small $\Delta\Omega_{cal,60}$, the external surface of the carapace was characterized by predominantly smooth surfaces, the absence of dissolution, and the presence of setae (Figs. 7 and S2). Ridging features were present on all examined carapaces but significantly increased at the stations with the greatest $\Delta\Omega_{cal,60}$ difference (Figs. 4 and 5). This presence of ridging features co-occurred with the increased occurrence of crystal exposure, ranging from increased porosity (Stage 1) to exposed crystals (Stage 2) at the sites with lower $\Delta\Omega_{cal,60}$ difference, and deeper-protruding dissolution at the sites with greater $\Delta\Omega_{cal,60}$ difference (Stage 2). Using image analysis, the depth of ridging structures was estimated at approximately 2 μm, around 25% of the cuticle thickness. Given the exocuticle thickness of 2–3 μm, the dissolution extended into the endocuticle (Fig. 6). The extent of dissolution on pereopod exoskeleton was comparable with the external dissolution, especially at the higher dissolution values (Fig. S5; $R^2 = 0.65$; $p = .0047$, slope = 0.901), indicating that both features were reliable metrics for dissolution assessment.

There was a distinct pattern of severe dissolution specifically developed around the calcified neuritic canals (Fig. 6). In megalopae collected at inshore stations (<200 m bottom depth), the carapace surface around the neuritic canals was markedly dissolved (Stage 2), and mechanoreceptors were often absent. Dissolution around the neuritic canals appeared to alter the morphology of the setae (Fig. 6). Setae edges were partially collapsed at the places where the mechanoreceptors are anchored in, with the initial ridging features around the canals degenerated into severely dissolved surfaces at the more intense $\Delta\Omega_{cal,60}$ values (Fig. 6). On the megalopae from offshore stations with a smaller $\Delta\Omega_{cal,60}$ the mechanoreceptors were present with no damage around the neuritic canals and less severe dissolution. Within the region of altered setae, dissolution up to 2–3 μm around the setae (Fig. S4) was accompanied by significant canal deformation. This deformation appears to destabilize the attachment of the setae anchor, resulting in the setae 'outrooting'. In some of the calcified neuritic canals, we noted the absence of setae but have not yet quantified the frequency of this occurrence.

To examine whether external or internal dissolution affects organismal or even potentially population-level metrics, dissolution measures were compared to megalopae body parameters and abundance. Here, we made an assumption that all the larval were released at the same time to be able to compare different length parameters. We detected a significant negative correlation between external dissolution and width, as indicated by reduced individual carapace width (CW; $F = 18.61$, $R^2 = 0.823$, $p = .013$ for the regression of CW against external dissolution on body parts; $F = 5.3$, $R^2 = 0.57$, $p = .08$ for the regression of CW against all external dissolution; Fig. 5d), which is particularly strong in the coastal stations. This demonstrates that external OA-related exposure can indirectly result in reduced larval width. Carapace width was strongly oriented along the first RDA axis (Fig. 3), while being orthogonal to internal dissolution and directly opposed to external dissolution. The latter aligns with previous findings that internal dissolution is uncoupled from carapace width (linear model $p > .05$), whereas external dissolution is significantly associated with carapace width (RDA plot). Other length-related parameters (CL, R-DCS, TL) were not affected by OA parameters, demonstrating that only specific body parameters, *i.e.*, width are affected at more severe $\Delta\Omega_{cal,60}$ vertical gradients.

On the higher, population-level response, only chl-a was found to be a significant driver. Abundance was positively correlated with chl-a at 60 m depth for both onshore and offshore habitats ($R^2 = 0.327$; $p = .008$). None of the other environmental parameters had a significant impact. However, in shallow coastal habitats with depth < 30 m, temperature was negatively related to larval abundance (for temperature at 10 m, $R^2 = 0.241$; $p = .02$; $F = 6.56$), although chl-a remained the dominant driver. In addition, neither carapace dissolution nor the width was related to larval abundance, suggesting decoupling of individual- and population-level effects of environmental conditions on larval Dungeness during the present day.

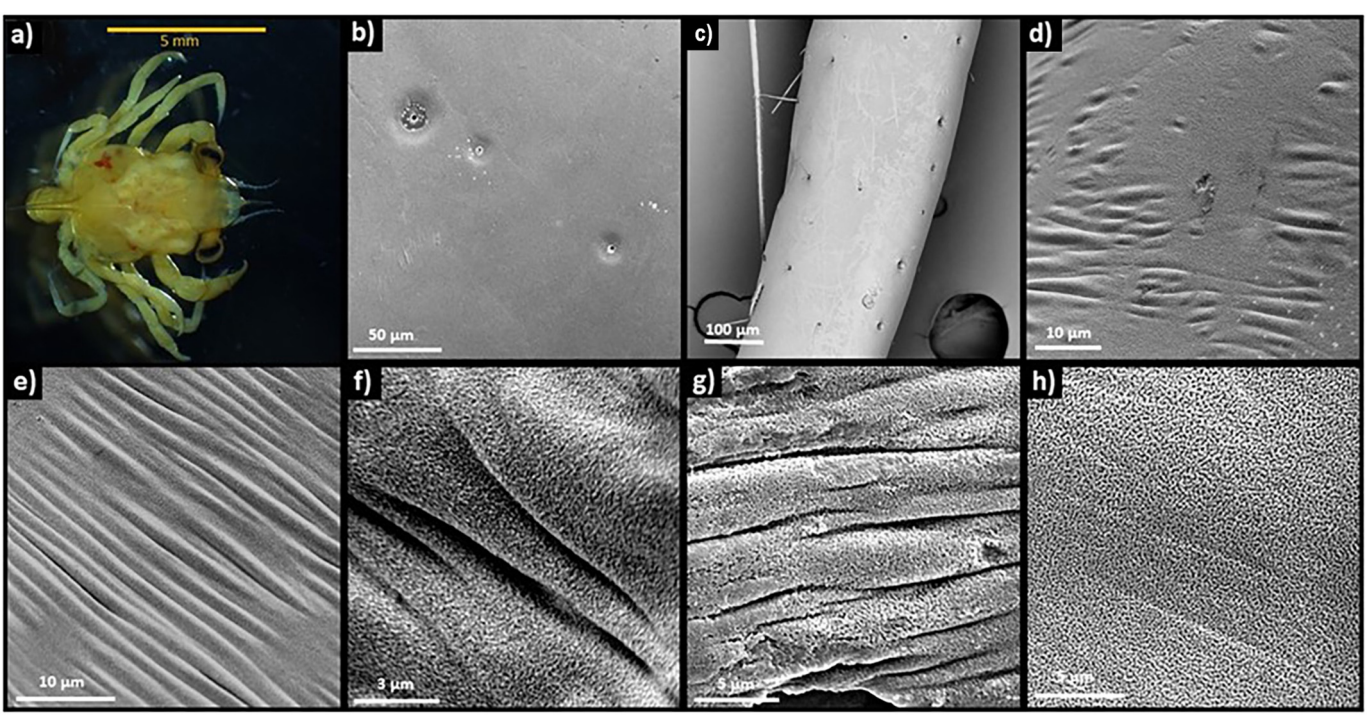

Fig. 4. External carapace and pereopod exoskeleton of the Dungeness crab megalopae (*a*) in its undamaged form (*b, c*) and with dissolution presence ranging from mild (Stage 1; *d*) to severe (Stage 2; *e, f*) patterns showing similarity in the structural damages (*g*) or exposed crystals (*h*). Indicated is the scale of the measurements (μm). The undamaged megalopae originated from the offshore or northwards habitats characterized by low $\Delta\Omega_{cal,60}$ vertical gradients, while the most severely affected megalopae came from the nearshore or coastal habitats with steep $\Delta\Omega_{cal,60}$ conditions. See more detailed explanation of the exoskeleton dissolution in the Supplementary Figs. S2, S3.

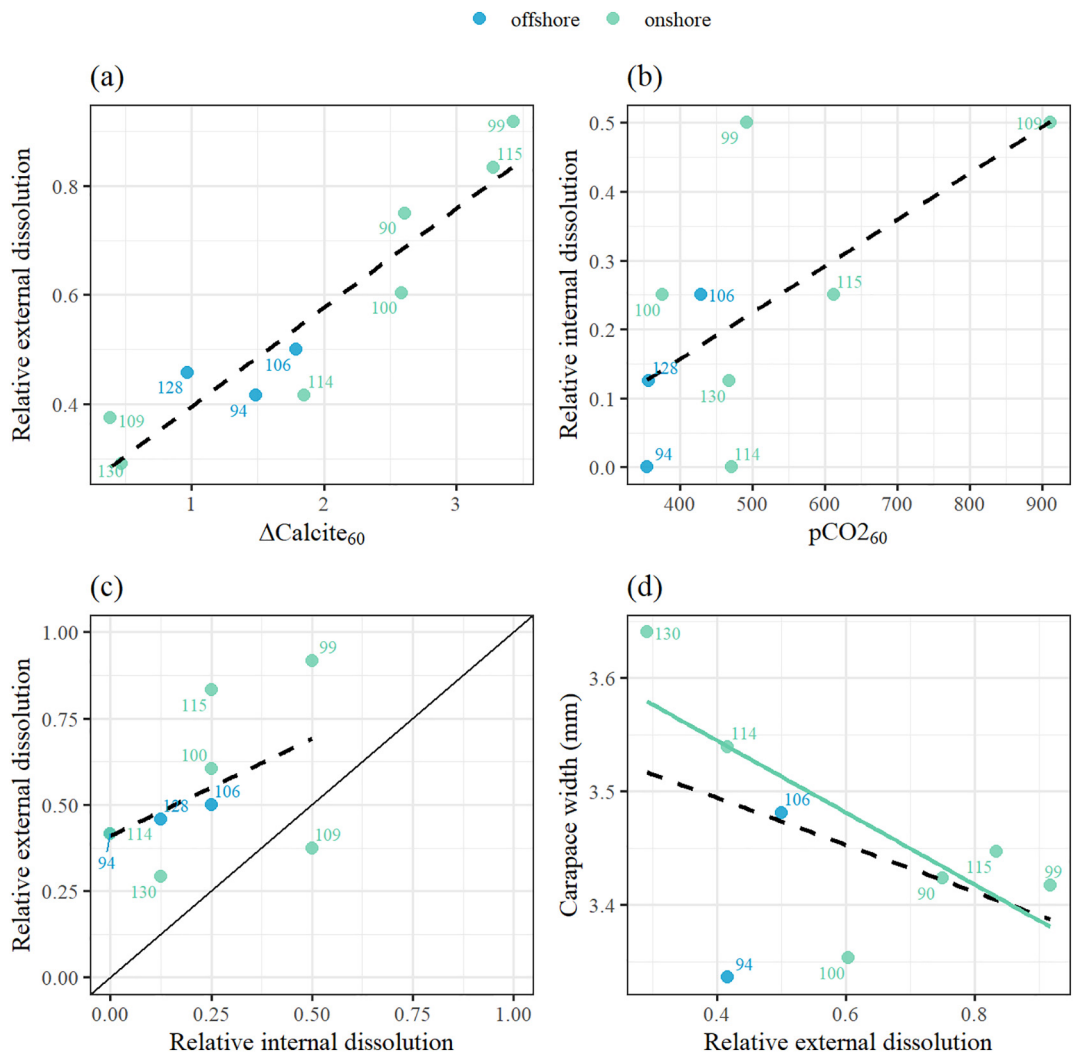

Fig. 5. Estimated linear relationships between ocean-acidification conditions and dissolution. Specifically for *a*) $\Delta\Omega_{cal,60}$ and relative external dissolution ($R^2 = 0.87$; $p < .001$) with the equation of relative external dissolution $= 0.181^*\Delta\Omega_{cal,60} + 0.215$; *b*) Depth-integrated $pCO_{2,60}$ and relative internal dissolution ($R^2 = 0.41$; $p = .064$); *c*) Comparison of the relative external and internal dissolution ($R^2 = 0.24$; $p = .18$); and *d*) Relative external dissolution and carapace width ($R^2 = 0.57$; $p = .08$). Dotted lines show the linear regression fit between all points. The solid line in (*c*) is the 1:1 line and the green line in (*d*) is the regression fit only through the onshore points. See methods for explanation of the term relative dissolution. Carapace width is in mm. (For interpretation of the references to colour in this figure legend, the reader is referred to the web version of this article.)

3.4. Megalopae exposure history to coastal OA conditions during the month prior to sampling

Particle back-tracking results with simulated vertical migration between the ocean surface and 60 m depth over a 30-d period from the J-SCOPE simulations showed that megalopae that were released in coastal habitats (<200 m), remained in coastal habitat for nearly a month of simulation regardless of their position in the domain (Fig. 7). This retention results in extended exposure to steeper coastal vertical gradients in OA conditions (Fig. 2), and consequently, more intense dissolution (Fig. 5).

4. Discussion

To our knowledge this is the first time that OA-related dissolution of calcite structures *in situ* has been demonstrated for crustaceans. Our results indicate that it is the exposure to both parameters, $\Delta\Omega_{cal,60}$ (*i.e.* the difference in calcite saturation depth between the surface and 60 m depth) and pCO_2, set up by as well as prolonged (<1 month) retention in the coastal waters that characterizes the suite of *in situ* parameters determining the larval crab vulnerability. This primarily demonstrates that it is not just the mean state OA conditions, but also the vertical difference in the water column that can induce negative biological responses. Using a retrospective prediction from a regression model (Fig. 5a), we estimate an 8.3% increase in the extent of external carapace dissolution over the last two decades. This post-hoc estimate was based on a ΔpH changes of 0.02 unit per decade (Carter et al., 2018), comparing current average with the extent of dissolution predicted from our regression model based on the *in situ* observations (Fig. 5a with the equation in the figure content) by using the estimated pH conditions two decades prior. This is a reasonable estimate since $\Delta\Omega_{cal,60}$ is highly correlated with $\Delta\Omega_{pH,60}$ ($F = 204.3$, $R^2 = 0.96$, $p < .001$, Fig. S6).

What makes this OA-dependent dissolution of megalopae particularly relevant is that the crab samples originated in the supersaturated conditions with respect to calcite (the lowest $\Omega_{calc} = 1.41$). Since the dissolution reported in other calcifiers has been demonstrated above Ω_{ara} of 1.4–1.5 (Bednaršek and Ohman, 2015; Bednaršek et al., 2016), we conclude that exoskeleton dissolution is initiated at higher $\Delta\Omega_{cal,60}$ than predicted based on thermodynamic principles alone. Furthermore, using exposure metrics based on the biogeochemical model output demonstrates that 1-month long exposure in coastal habitats with large $\Delta\Omega_{cal,60}$ values can result in significantly more dissolution than predicted based on snap-shot observational data. In comparison with

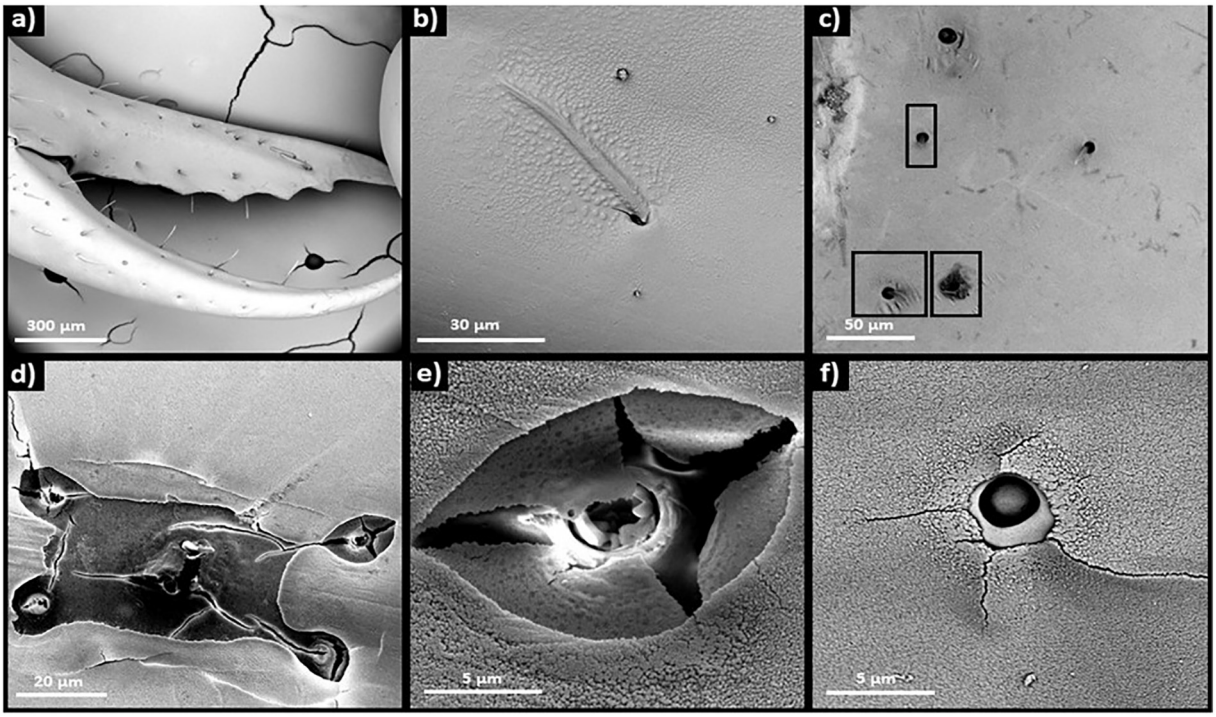

Fig. 6. Presence of setae on the pereopods (*a*) and carapace surface (*b*) of the megalopae on the intact individuals. The exposure to greater $\Delta\Omega_{cal,60}$ differences mechanically damages the setae and results in their absence and outrooting (black squares) because of the dissolution around the neuritic canals (*d*, *f*) and damage with the collapsed structure (*e*).

the chemical observations, particle tracking model output indicates prolonged severity of exposure to the coastal low OA conditions, allowing for more extensive exoskeleton dissolution and reduced larval width in those habitats. It is worth noting that dissolution could be viewed as a physiological strategy to compensate against unfavorable external conditions. Dissolution of the outer calcite layer could increase the release of the bicarbonate and hydroxyl ions, raising pH, and providing a rapid alkalinization of the superficial layer (Kunkel et al., 2012). This alkaline layer could then provide an additional local protection from exposure to a large $\Delta\Omega_{cal,60}$ conditions by blocking protons from continuously invading the internal fluid However, as the larvae live in highly dynamic environments, such a layer would be continuously disrupted, explaining the high extent of external dissolution.

4.1. Dissolution as a mechanism to offset OA-related extracellular acid-base disturbance?

Species with a developed capacity for ion exchange to maintain extracellular acid-base balance, are able to compensate for the effects of exposure to high pCO_2 waters and restore extracellular pH values optimal for physiological and biogeochemical processes (Somero, 1986). They do so *via* energetically expensive buffering of intra- and

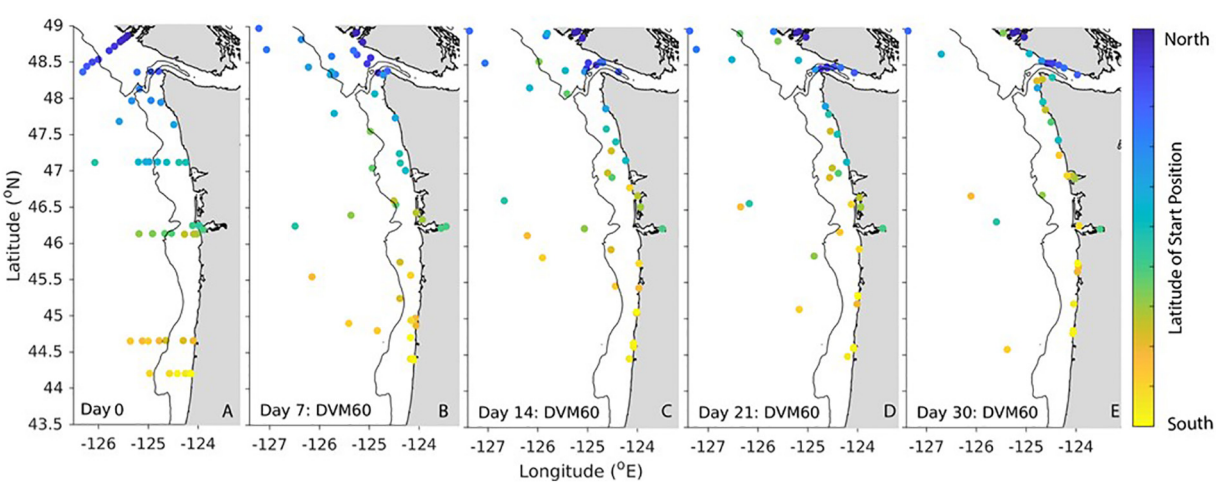

Fig. 7. Particle initialization locations (*a*) and average backtracked locations (*b*-*e*) for 7, 14, 21, and 30-day simulated particles exhibiting diel vertical migration (DVM) between 0 and 60 m depths. Replicate particles ($n = 100$) were initialized in the model at 51 locations representing the sampling stations for the 2016 West Coast Ocean Acidification Cruise. J-SCOPE's historical simulation of ocean conditions for 2016 was used to simulate advection of particles, and each particle exhibited vertical swimming between the ocean surface at night and a maximum daytime depth of 60 m. On a weekly basis, particle locations were averaged for all 100 particles initialized at the same station, which sometimes resulted in the average location being on land. These particles were moved to the nearest shoreline. Station colour varies by transect for improved resolution of dispersal patterns occurring at different latitudes. The 200 m isobath is shown for reference, and land is shaded in grey.

extracellular compartments achieved through various mechanisms, such as buffering by seawater-derived bicarbonate sources (Truchot, 1979), and increased respiratory activity to reduce CO_2 loading of the extracellular fluid and non-bicarbonate buffering (Cameron, 1985; Hans et al., 2014; Michaelidis et al., 2005).

However, the downside to the well-established extracellular acid-base control is an energetically demanding process (Hans et al., 2014; Michaelidis et al., 2005; Pane and Barry, 2007; Trigg et al., 2019). Therefore, we hypothesize that the internal carapace dissolution we observed in our study could be a part of a passive ability to buffer reductions in extracellular pH, a feature found in a variety of marine invertebrates including bivalves, echinoderms, and crustaceans (Cameron, 1985; Henry et al., 1981; Lindinger et al., 1984; Spicer and Taylor, 1987; Spicer et al., 2007). The narrow neuritic canals around the mechanoreceptors allow communication through secretion across the internal-external cuticle layers (Kunkel et al., 2012).While we currently have no information on the acid-base balance within these larval crabs under prolonged exposure to steep pCO_2 vertical gradients because no controlled experiments have been conducted, we propose future studies to examine if internal dissolution could provide some level of bicarbonate ions for buffering at comparatively low cost.

Alternative hypothesis for explaining internal dissolution might be based on the severity of external dissolution extending much deeper (Fig. S4) to initiate the endocuticle dissolution. Once the dissolution of the external carapace dissolution is initiated, the mineralogical-elemental structure of the mid- and endocuticle can allow for more rapid progression. The presence of high-Mg^{2+} content in the endocuticle can cause more rapid dissolution (Andersson et al., 2008), while comparatively lower Ca^{2+} content on the outward side presumably results in a weaker carapace (Chen et al., 2008). In addition, chitin-proteinaceous matrix, such as an amorphous crystalline layer might be present, which could importantly contribute to additional dissolution. Furthermore, while the internal solubility extent may be compensated by phosphorus, it can increase hardness, thereby preventing propagation of fractures, and Sr^{2+} because it can replace Ca^{2+} in the mineralization process (Dodd, 1964). In contrast, the observation of less internal dissolution on the endocuticle side compared to the external dissolution could be due to a difference in biomineral composition. For instance, intermixing calcite in the endocuticle with organic polymers would create a durable, protective covering, which may prevent the more soluble high-Mg calcite in the endocuticle from dissolving (Chen et al., 2008). However, we have no observations of dissolution penetration all the way from the external to the internal side, we thus propose an acid-base balance strategy to be more feasible explanation for the internal dissolution.

4.2. Potential detrimental effect associated with carapace dissolution

One of the most important findings of this study is the correlation between carapace dissolution and the reduction in larval width. This could, overtime, potentially impact population dynamics. We suggest that the dissolution-length linkage could be explained by two different hypotheses: first, pronounced dissolution under severe $\Delta\Omega_{cal,60}$ vertical gradients results in dissolution rate outpacing calcification rate. In this mismatch of rates of two different processes, calcification rate cannot fully compensate for dissolution and results in overall smaller width ('*the mismatch*' hypothesis). Alternatively, there could be an energetic implication behind the dissolution-induced slowdown in width. In this form of the hypothesis, an organism expends additional energy to increase calcification to counteract dissolution, thus resulting in an energetic trade-off that potentially compromises organismal growth (the '*trade-off*' hypothesis).

Furthermore, for early Dungeness crab life stages in the near-future, the prediction of more frequent and prolonged exposures to more severe $\Delta\Omega_{cal,60}$ gradients (Turi et al., 2016) could have potentially deleterious consequences in terms of behavioral and sensory impairments and chelae function. First, dissolution-affected thinner structures may become too weak to retain their integrity, particularly under more severe conditions and continuous water flow, resulting in ridged, puffed surfaces. Morphological changes may in turn negatively impact larval survival by altering swimming behaviors and competence, including the ability to regulate buoyancy, maintain vertical position, and avoid predators (Morgan, 1989; Sulkin, 1984). Similar morphological structures as those observed in our study were noted in the larval form of the European lobster (Agnalt et al., 2013), which under prolonged exposure to OA conditions led to irreparable carapace deformities, and these could lead to an increase in molt-related mortalities (Small et al., 2016). Second, dissolution on both sides of carapace and pereopod exoskeleton will inevitably limit the effectiveness of the exoskeleton in providing support for muscles contraction and defense from predators, aiding homeostatic functions, and enabling feeding functions. Third, calcified neuritic canals appear to be one of the dissolution hotspots compromising setae function. Compared with undamaged setae at undissolved surfaces (Figs. 6 and S2, S3), dissolved areas may not provide sufficient structural integrity for the setae (Fig. 6), potentially impairing their functionality. Given the role of setae as mechanoreceptors directly involved in supporting crustacean sensory and behavior processes, we hypothesize that the absence or damage of setae within their neuritic canals may in part provide a mechanistic understanding for potential aberrant behavioral patterns found across various crustacean species under low OA conditions, such as slower movement, less tactile recognition, and prolonged searching time, as well as impaired swimming (Alenius and Munguia, 2012; Dissanayake and Ishimatsu, 2011) and behavioral choice (de la Haye et al., 2011). These changes can result in impaired competitiveness and altered predator-prey relationships for crabs (de la Haye et al., 2012; Dodd et al., 2015; Landes and Zimmer, 2012; Wang et al., 2018). Fourth, it is currently unknown whether external dissolution in megalopae could carry over into later life stages, including the reproductively active adult stage, and what the potential consequences may be for the population dynamics. However, reduced calcification could result in poor mineralization through the intermolt period that would be especially devastating for larval crabs because of potentially smaller sizes at maturity, as well as increased vulnerability to predation during their most sensitive molting stage.

While OA parameters largely affect observed biominerological and organismal responses, population-level responses (*i.e.* abundances) are driven by food availability, with a lesser role for temperature in the near-shore conditions. Although biological responses at different levels of biological organization appear to be decoupled and responded to different drivers across temporal and spatial scales that need to be taken into account to improve biological forecasts and predictions. The only driver that seem to resonate across individual and population level, at least marginally, is the temperature, which might have an opposite effect on both levels. While warmer temperature negatively affects abundances, it also reduces internal dissolution, although the latter is only a marginally significant.

To more accurately predict large-scale vulnerability, it is important to consider population connectivity, related to essential population vital rates and affected by dispersal (Lowe and Allendorf, 2010). This can be partitioned into genetic connectivity and demographic connectivity, with our model outputs demonstrating onshore-offshore connectivity along the shelf-coastal and in the northern-southern directions. This implies prolonged exposure to less suitable habitats characterized by low $\Delta\Omega_{cal,60}$ in the nearshore areas that can exacerbate negative biological effects but some of them could be counteracted by higher food availability. With respect to genetic connectivity, the status of Dungeness crab as a high gene-flow species with low genetic differentiation along the US West Coast and the lack of significant adaptation patterns (Jackson and O'Malley, 2017; Jackson et al., 2018; O'Malley et al., 2017) implies that the genetic pool that might allow for adaptation under future climate scenario will be limited. This points toward the need for more comprehensive population vulnerability assessment that can link OA vulnerability with the population genetics.

4.3. Future directions

Like dissolution in pteropods, larval dissolution observed in Dungeness crab is clear evidence that marine invertebrates are damaged by extended exposure to strong present-day OA-related vertical gradients in their natural environment. The unexplored aspect of OA impacts related to the damaged mechanoreceptors and potentially impaired sensory functions needs to be explored further. Namely, if the sensory functions are impaired, the transitioning from the larval to juvenile stage in their coastal habitat might be compromised under predicted scenarios of steeper ΔpH and $\Delta\Omega_{cal,60}$ gradients (Gruber et al., 2012; Turi et al., 2016). Multiple pathways of larval vulnerability should be studied in the context of carry-over effects to the next juvenile benthic stage to explore whether crustacean molting can offset some of the detrimental effects. Such findings should be integrated into a population demographic and exposure history model that could eventually lead to improved management of Dungeness crab stocks (Fernandes et al., 2017; Lam et al., 2016).

Declaration of competing interest

The authors declare that they have no known competing financial interests or personal relationships that could have appeared to influence the work reported in this paper.

Acknowledgements

We thank Carry Weekes and Anna McLasky for collecting the larval individuals, Jennifer Fisher for providing guidance to Carry Weekes; Sten Littmann from Max Planck Institute in Bremen, Germany for elemental analyses. We are grateful to Polona Mrak and Miloš Vittori for analyses of the crab molting stages. We thank to Sandra Bigley for her editorial help with the manuscript.

Funding sources

This work was supported by the NOAA's Ocean Acidification Program for initial funding and NOAA Pacific Marine Environmental Laboratory (PMEL) for supporting NB, RAF, SRA, and SAS. This is PMEL contribution number 4906.

Appendix A. Supplementary data

Supplementary data to this article can be found online at https://doi.org/10.1016/j.scitotenv.2020.136610.

References

Agnalt, A.-L., Grefsrud, E.S., Farestveit, M., Larsen, M., Keulder, F., 2013. Deformities in larvae and juvenile European lobster (*Homarus gammarus*) exposed to lower pH at two different temperatures. Biogeosciences 10, 7883–7895.

Akaike, H., 1973. Information theory and an extension of the maximum likelihood principle. In: Petrov, B.N., Csaki, F. (Eds.), Second International Symposium on Information Theory. Akademiai Kiado, Budapest, Hungary, pp. 267–281.

Alenius, B., Munguia, P., 2012. Effects of pH variability on the intertidal isopod, *Paradella dianae*. Mar. Freshw. Behav. Physiol. 45, 245–259.

Andersson, A.J., Mackenzie, F.T., Bates, N.R., 2008. Life on the margin: implications of ocean acidification on mg-calcite, high latitude and cold-water marine calcifiers. Mar. Ecol. Prog. Ser. 373, 265–273.

Bednaršek, N., Ohman, M.D., 2015. Changes in pteropod distributions and shell dissolution across a frontal system in the California current system. Mar. Ecol. Prog. Ser. 523, 93–103.

Bednaršek, N., Tarling, G.A., Bakker, D.C., Fielding, S., Cohen, A., Kuzirian, A., McCorkle, D., Lézé, B., Montagna, R., 2012. Description and quantification of pteropod shell dissolution: a sensitive bioindicator of ocean acidification. Glob. Chang. Biol. 18, 2378–2388.

Bednaršek, N., Feely, R.A., Reum, J.C.P., Peterson, B., Menkel, J., Alin, S.R., Hales, B., 2014. *Limacina helicina* shell dissolution as an indicator of declining habitat suitability owing to ocean acidification in the California current ecosystem. Proc. R. Soc. B Biol. Sci. 281, 20140123.

Bednaršek, N., Johnson, J., Feely, R.A., 2016. Comment on peck et al: vulnerability of pteropod (*Limacina helicina*) to ocean acidification: Shell dissolution occurs despite an intact organic layer. Deep-Sea Research Part II: Topical Studies in Oceanography 127, 53–56.

Bednaršek, N., Feely, R.A., Tolimieri, N., Hermann, A.J., Siedlecki, S.A., Waldbusser, G.G., McElhany, P., Alin, S.R., Klinger, T., Moore-Maley, B., Pörtner, H.O., 2017. Exposure history determines pteropod vulnerability to ocean acidification along the US west coast. Sci. Rep. 7, 4526.

Busch, D.S., McElhany, P., 2016. Estimates of the direct effect of seawater pH on the survival rate of species groups in the California current ecosystem. PLoS One 11, e0160669.

Cameron, J.N., 1985. Compensation of hypercapnic acidosis in the aquatic blue crab, *Callinectes sapidus*: the predominance of external sea water over carapace carbonate as the proton sink. J. Exp. Biol. 114, 197–206.

Carter, H.A., Ceballos-Osuna, L., Miller, N.A., Stillman, J.H., 2013. Impact of ocean acidification on metabolism and energetics during early life stages of the intertidal porcelain crab Petrolisthes cinctipes. J. Exp. Biol. 216 (8), 1412–1422.

Carter, B.R., Feely, R.A., Williams, N.L., Dickson, A.G., Fong, M.B., Takeshita, Y., 2018. Updated methods for global locally interpolated estimation of alkalinity, pH, and nitrate. Limnology and Oceanography Methods 16 (2), 119–131.

Chavez, F., Pennington, J.T., Michisaki, R.P., Blum, M., Chavez, G.M., Friederich, J., Messié, M., 2017. Climate variability and change: response of a coastal ocean ecosystem. Oceanography 30, 128–145.

Chen, P.-Y., Lin, A.Y.-M., McKittrick, J., Meyers, M.A., 2008. Structure and mechanical properties of crab exoskeletons. Acta Biomater. 4, 587–596.

Davis, S., Sylvia, G., Yochum, N., Cusack, C., 2017. Oregon Dungeness Crab Fishery Bioeconomic Model: A Fishery Interactive Simulator Learning Tool. Version 5.7. Prepared by Coastal Oregon Marine Experiment Station, Oregon State University and the Research Group, LLC for the Oregon Dungeness Crab Commission.

de la Haye, K.L., Spicer, J.I., Widdicombe, S., Briffa, M., 2011. Reduced Sea water pH disrupts resource assessment and decision making in the hermit crab *Pagurus bernhardus*. Anim. Behav. 82, 495–501.

de la Haye, K.L., Spicer, J.I., Widdicombe, S., Briffa, M., 2012. Reduced pH sea water disrupts chemo-responsive behaviour in an intertidal crustacean. J. Exp. Mar. Biol. Ecol. 412, 134–140.

Dissanayake, A., Ishimatsu, A., 2011. Synergistic effects of elevated CO_2 and temperature on the metabolic scope and activity in a shallow-water coastal decapod (*Metapenaeus joyneri*; Crustacea: Penaeidae). ICES J. Mar. Sci. 68, 1147–1154.

Dodd, J.R., 1964. Environmentally controlled variation in the shell structure of a pelecypod species. J. Paleontol. 38, 1065–1071.

Dodd, L.F., Grabowski, J.H., Piehler, M.F., Westfield, I., Ries, J.B., 2015. Ocean acidification impairs crab foraging behaviour. Proc. R. Soc. B Biol. Sci. 282, 20150333.

Fabritius, H.O., Karsten, E.S., Balasundaram, K., Hild, S., Huemer, K., Raabe, D., 2012. Correlation of structure, composition and local mechanical properties in the dorsal carapace of the edible crab *Cancer pagurus*. Z. Krist. 227 (11), 766–776.

Feely, R.A., Alin, S., Carter, B., Bednaršek, N., Hales, B., Chan, F., Juranek, L., 2016. Chemical and biological impacts of ocean acidification along the west coast of North America. Estuar. Coast. Shelf Sci. 183, 260–270.

Feely, R.A., Okazaki, R.R., Cai, W.-J., Bednaršek, N., Alin, S.R., Byrne, R.H., Fassbender, A., 2018. The combined effects of acidification and hypoxia on pH and aragonite saturation in the coastal waters of the California current ecosystem and the northern Gulf of Mexico. Cont. Shelf Res. 152, 50–60.

Fernandes, J.A., Papathanasopoulou, E., Hattam, C., Queirós, A.M., Cheung, W.W., Yool, A., Artioli, Y., Pope, E.C., Flynn, K.J., Merino, G., Calosi, P., Beaumont, N., Austen, M.C., Widdicombe, S., Barange, M., 2017. Estimating the ecological, economic and social impacts of ocean acidification and warming on UK fisheries. Fish Fish. 18, 389–411.

Fox, J., Weisberg, S., 2011. An R Companion to Applied Regression. SAGE Publications, USA.

Giltz, S.M., Taylor, C.M., 2017. Reduced growth and survival in the larval blue crab *Callinectes sapidus* under predicted ocean acidification. J. Shellfish Res. 36, 481–485.

González-Gordillo, J.I., Rodríguez, A., Queiroga, H., 2004. Characterization of the megalopal premoult stages of the green crab, *Carcinus Maenas* (Decapoda, Portunidae), from laboratory culture. J. Crustac. Biol. 24, 502–510.

Gravinese, P.M., Enochs, I.C., Manzello, D.P., van Woesik, R., 2018. Warming and pCO_2 effects on Florida stone crab larvae. Estuar. Coast. Shelf Sci. 204, 193–201.

Gruber, N., Hauri, C., Lachkar, Z., Loher, D., Frölicher, T.L., Plattner, G.-K., 2012. Rapid progression of ocean acidification in the California current system. Science 337, 220–223.

Hans, S., Fehsenfeld, S., Treberg, J.R., Weihrauch, D., 2014. Acid–base regulation in the Dungeness crab (*Metacarcinus magister*). Mar. Biol. 161, 1179–1193.

Henry, R.P., Kormanik, G.A., Smatresk, N.J., Cameron, J.N., 1981. The role of $CaCO_3$ dissolution as a source of HCO_3^- for the buffering of hypercapnic acidosis in aquatic and terrestrial decapod crustaceans. J. Exp. Biol. 94, 269–274.

Hobbs, R.C., Botsford, L.W., Thomas, A., 1992. Influence of hydrographic conditions and wind forcing on the distribution and abundance of Dungeness crab, *Cancer magister*, larvae. Can. J. Fish. Aquat. Sci. 49, 1379–1388.

Hodgson, E.E., Kaplan, I.C., Marshall, K.N., Leonard, J., Essington, T.E., Busch, D.S., Fulton, E.A., Harvey, C.J., Hermann, A.J., McElhany, P., 2018. Consequences of spatially variable ocean acidification in the California current: lower pH drives strongest declines in benthic species in southern regions while greatest economic impacts occur in northern regions. Ecol. Model. 383, 106–117.

Jackson, T.M., O'Malley, K.G., 2017. Comparing genetic connectivity among Dungeness crab (*Cancer magister*) inhabiting Puget Sound and coastal Washington. Mar. Biol. 164 (6), 123.

Jackson, T.M., Roegner, G.C., O'Malley, K.G., 2018. Evidence for interannual variation in genetic structure of Dungeness crab (*Cancer magister*) along the California current system. Mol. Ecol. 27 (2), 352–368.

Kaplan, I.C., Williams, G.D., Bond, N.A., Hermann, A.J., Siedlecki, S.A., 2016. Cloudy with a chance of sardines: forecasting sardine distributions using regional climate models. Fish. Oceanogr. 25, 15–27.

Kunkel, J.G., Nagel, W., Jercinovic, M.J., 2012. Mineral fine structure of the American lobster cuticle. J. Shellfish Res. 31, 515–526.

Lam, V.W.Y., Cheung, W.W.L., Reygondeau, G., Sumaila, U.R., 2016. Projected change in global fisheries revenues under climate change. Sci. Rep. 6, 32607.

Landes, A., Zimmer, M., 2012. Acidification and warming affect both a calcifying predator and prey, but not their interaction. Mar. Ecol. Prog. Ser. 450, 1–10.

Lindinger, M.I., Lauren, D.J., Mcdonald, D.G., 1984. Acid-base balance in the sea mussel, *Mytilus edulis*. III. Effects of environmental hypercapnia on intra- and extracellular acid-base balance. Marine Biology Letters 5, 371–381.

Long, W.C., Swiney, K.M., Foy, R.J., 2016. Effects of high pCO_2 on Tanner crab reproduction and early life history, part II: carryover effects on larvae from oogenesis and embryogenesis are stronger than direct effects. ICES J. Mar. Sci. 73 (3), 836–848.

Lowe, W.H., Allendorf, F.W., 2010. What can genetics tell us about population connectivity? Mol. Ecol. 19, 3038–3051.

Manno, C., Rumolo, P., Barra, M., d'Albero, S., Basilone, G., Genovese, S., Mazzola, S., Bonanno, A., 2019. Condition of pteropod shells near a volcanic CO_2 vent region. Mar. Environ. Res. 143, 39–48.

Melzner, F., Gutowska, M.A., Langenbuch, M., Dupont, S., Lucassen, M., Thorndyke, M.C., Bleich, M., Pörtner, H.O., 2009. Physiological basis for high CO_2 tolerance in marine ectothermic animals: pre-adaptation through lifestyle and ontogeny? Biogeosciences 6 (3), 4693–4738.

Michaelidis, B., Ouzounis, C., Paleras, A., Pörtner, H., 2005. Effects of long-term moderate hypercapnia on acid-base balance and growth rate in marine mussels *Mytilus galloprovincialis*. Mar. Ecol. Prog. Ser. 293, 109–118.

Miller, J.J., Maher, M., Bohaboy, E., Friedman, C.S., McElhany, P., 2016. Exposure to low pH reduces survival and delays development in early life stages of Dungeness crab (*Cancer magister*). Mar. Biol. 163, 118.

Morgan, S.G., 1989. Adaptive significance of spination in estuarine crab Zoeae. Ecology 70, 464–482. https://doi.org/10.2307/1937551.

North, E.W., Schlag, Z., Hood, R.R., Li, M., Zhong, L., Gross, T., Kennedy, V.S., 2008. Vertical swimming behavior influences the dispersal of simulated oyster larvae in a coupled particle-tracking and hydrodynamic model of Chesapeake Bay. Mar. Ecol. Prog. Ser. 359, 99–115.

North, E.W., Adams, E.E., Schlag, Z., Sherwood, C.R., He, R., Hyun, K.H., Socolofsky, S.A., 2011. Simulating oil droplet dispersal from the *Deepwater Horizon* spill with a Lagrangian approach. In: Liu, Y., Macfadyen, A., Ji, Z., Weisberg, R.H. (Eds.), Monitoring and Modeling the Deepwater Horizon Oil Spill: A Record Breaking Enterprise. Geophysical Monograph Series. American Geophysical Union, USA, pp. 217–226.

Norton, E., Siedlecki, S.A., Kaplan, I.C., Hermann, A.J., Fisher, J., Morgan, C., Officer, S., Saenger, C., Alin, S.A., Newton, J.A., Bednaršek, N., Feely, R.A., 2020. The importance of environmental exposure history in forecasting Dungeness crab megalopae occurrence using J-SCOPE, a high-resolution model for the US Pacific northwest. Front. Mar. Sci. (*in revision*).

Oksanen, J., Blanchet, F.G., Friendly, M., Kindt, R., Legendre, P., McGlinn, D., Wagner, H., 2019. Vegan: Community Ecology Package. R Package Version 2.5–5. Available at. https://CRAN.R-project.org/package=vegan.

O'Malley, K.G., Corbett, K., Beacham, T.D., Jacobson, D.P., Jackson, T.M., Roegner, G.C., 2017. Genetic connectivity of the Dungeness crab (*Cancer magister*) across oceanographic regimes. J. Shellfish Res. 36 (2), 453–465.

Pacific States Marine Fisheries Commission, 2019. Species Report: Commercial Land Catch: Metric-Tons (Mt), Revenue, and Price-per-Pound (Price/Lbs). Pacific States Marine Fisheries Commission, Portland, OR Available at. https://reports.psmfc.org/pacfin/f?p=501:1:5808950816361::NO::, Accessed date: 25 March 2019.

Paganini, A.W., Miller, N.A., Stillman, J.H., 2014. Temperature and acidification variability reduce physiological performance in the intertidal zone porcelain crab *Petrolisthes cinctipes*. J. Exp. Biol. 217 (22), 3974–3980.

Page, T.M., Worthington, S., Calosi, P., Stillman, J.H., 2016. Effects of elevated pCO_2 on crab survival and exoskeleton composition depend on shell function and species distribution: a comparative analysis of carapace and claw mineralogy across four porcelain crab species from different habitats. ICES J. Mar. Sci. 74 (4), 1021–1032.

Pane, E., Barry, J., 2007. Extracellular acid-base regulation during short-term hypercapnia is effective in a shallow-water crab, but ineffective in a deep-sea crab. Mar. Ecol. Prog. Ser. 334, 1–9.

R Core Team, 2019. R: A Language and Environment for Statistical Computing. R Foundation for Statistical Computing Available at. https://www.R-project.org/.

Schiffer, M., Harms, L., Pörtner, H., Mark, F., Storch, D., 2014. Pre-hatching seawater pCO_2 affects development and survival of zoea stages of Arctic spider crab *Hyas araneus*. Mar. Ecol. Prog. Ser. 501, 127–139.

Schlag, Z.R., North, E.W., 2012. Lagrangian TRANSport model (LTRANS v.2) User's Guide. University of Maryland Center for Environmental Science, Horn Point Laboratory, Cambridge, Maryland.

Shanks, A.L., 1995. Mechanisms of cross-shelf dispersal of larval invertebrates and fish. In: McEdward, L.R. (Ed.), Ecology of Marine Invertebrate Larvae. CRC Press, USA, pp. 324–367.

Siedlecki, S.A., Kaplan, I.C., Hermann, A.J., Nguyen, T.T., Bond, N.A., Newton, J.A., Williams, G.D., Peterson, W.T., Alin, S.R., Feely, R.A., 2016. Experiments with seasonal forecasts of ocean conditions for the northern region of the California current upwelling system. Sci. Rep. 6, 27203.

Sinclair, M., 1988. Marine Populations: An Essay on Population Regulation and Speciation. Washington Sea Grant. University of Washington Press, Seattle, Washington.

Small, D.P., Calosi, P., Boothroyd, D., Widdicombe, S., Spicer, J.I., 2015. Stage-specific changes in physiological and life-history responses to elevated temperature and pCO_2 during the larval development of the European lobster *Homarus gammarus* (L.). Physiol. Biochem. Zool. 88, 494–507.

Small, D.P., Calosi, P., Boothroyd, D., Widdicombe, S., Spicer, J.I., 2016. The sensitivity of the early benthic juvenile stage of the European lobster *Homarus gammarus* (L.) to elevated pCO_2 and temperature. Mar. Biol. 163, 53.

Somero, G.N., 1986. Protons, osmolytes, and fitness of internal milieu for protein function. Am. J. Phys. Regul. Integr. Comp. Phys. 251, R197–R213.

Somero, G.N., Beers, J.M., Chan, F., Hill, T.M., Klinger, T., Litvin, S.Y., 2015. What changes in the carbonate system, oxygen, and temperature portend for the northeastern Pacific Ocean: a physiological perspective. BioScience 66, 14–26.

Spicer, J.I., Raffo, A., 2007. Widdicombe, S., iInfluence of CO_2-related seawater acidification on extracellular acid–base balance in the velvet swimming crab *Necora puber*. Mar. Biol. 151, 1117–1125.

Spicer, J.I., Taylor, A.C., 1987. Carbon dioxide transport and acid-base regulation in the blood of the beach-hopper *Orchestia gammarellus* (Pallas) (Crustacea: Amphipoda). Ophelia 28, 49–61.

Sulkin, S.D., 1984. Behavioral basis of depth regulation in the larvae of brachyuran crabs. Mar. Ecol. Prog. Ser. 15, 181–205.

Trigg, S.A., McElhany, P., Maher, M., Perez, D., Busch, D.S., Nichols, K.M., 2019. Uncovering mechanisms of global ocean change effects on the Dungeness crab (*Cancer magister*) through metabolomics analysis. BioRxiv 574798 (1 August).

Truchot, J.P., 1979. Mechanisms of the compensation of blood respiratory acid-base disturbances in the shore crab, *Carcinus maenas* (L.). J. Exp. Zool. 210, 407–416.

Tunnicliffe, V., Davies, K.T., Butterfield, D.A., Embley, R.W., Rose, J.M., Chadwick Jr., W.W., 2009. Survival of mussels in extremely acidic waters on a submarine volcano. Nat. Geosci. 2, 344–348.

Turi, G., Lachkar, Z., Gruber, N., Münnich, M., 2016. Climatic modulation of recent trends in ocean acidification in the California current system. Environ. Res. Lett. 11, 014007.

Wang, Y., Hu, M., Wu, F., Storch, D., Pörtner, H.-O., 2018. Elevated pCO_2 affects feeding behavior and acute physiological response of the Brown crab *Cancer pagurus*. Front. Physiol. 9, 1164.

U.S. Coast Guard Cutter *McCulloch*

Photo: Robert Schwemmer Maritime Library

U.S. Revenue Cutter *McCulloch* off Mare Island Navy Shipyard, San Francisco Bay, California, circa 1900.

Photo: USCG Historian's Office

U.S. Revenue Cutter *McCulloch*'s crew, date unknown.

Photos: San Francisco Maritime National Historical Park

Photos: (top) Passenger steamship SS *Governor.* (bottom): USCG Cutter *McCulloch* sinking by the bow after the collision with the SS *Governor.*

Early History

The U.S. Revenue Cutter *McCulloch* was named in honor of Hugh McCulloch, the 27th and 36th Secretary of the Treasury, under Presidents Abraham Lincoln, Andrew Johnson, and later, Chester A. Arthur and Grover Cleveland.

USRC *McCulloch* was constructed by William Cramp and Sons in Philadelphia, Pennsylvania. Launched in 1896, it was the largest cutter built to date at a cost of over $200,000. The hull was composition construction, where wood planks were mounted over steel framing. The cutter was commission into the Revenue Cutter Service on December 12, 1897, under the command of Captain D.B. Hogsdon, RCS. A single triple-expansion marine steam engine provided a cruising speed of 17 knots and to extend its range, *McCulloch* was barkentine rigged with three masts. *McCulloch*'s length was 219 feet, with a beam of 33.4 feet, depth of hold 17.1 feet, and displacement of 1,280 tons. The cutter's armament included four 6-pounder 3-inch guns and one 15-inch torpedo tube molded in the bow stem. During war time *McCulloch*'s complement was 130 crewmen.

In 1898, the cutter saw action at the Battle of Manila Bay under the command of Commodore George Dewey. Commodore Dewey would later, in a message to the Secretary of the Navy, commend Captain Hogsdon for the efficiency and readiness of his ship.

In January 1899, *McCulloch* arrived at San Francisco, California, and operated on patrol duty out of that port, cruising from the Mexican border to Cape Blanco, Oregon. The cutter later operated near the Pribilof Islands to enforce fur seal regulations. During these years in the Bering Sea Patrol, *McCulloch* became well known because of its services as a floating courtroom for far-flung Alaskan towns. *McCulloch* returned to San Francisco and resumed patrol duties off the west coast in 1912. In 1914, *McCulloch* was ordered to Mare Island Navy Shipyard where the cutter's boilers were replaced, the mainmast was removed and the bowsprit shortened.

In March 1917, *McCulloch* returned to Mare Island Navy Shipyard and went through overhauls that included removing 800 pounds of copper sheathing, and re-caulking the wooden hull. On April 6, 1917, *McCulloch* was put under U.S. Navy operational command for patrol duties at the onset of World War I. *McCulloch* maintained the distinction as the largest Revenue, and later Coast Guard cutter during its 20-year career, and was decommissioned on June 13, 1917.

USCG Cutter *McCulloch* Collision with the Passenger Steamship SS *Governor*

On June 13, 1917, the cutter was proceeding cautiously through dense fog on its trip from San Pedro, California to San Francisco. At 7:30 that morning, the cutter was four miles west-northwest of Point Conception when Captain John C. Cantwell, Commanding, and Ensign William Mayne, officer of the deck in charge of navigation, heard a steamer's fog signal off the starboard bow. Nearby, the passenger steamship *Governor* was southbound from San Francisco to San Pedro. Captain Howard C. Thomas, master of the *Governor*, heard *McCulloch*'s fog signal and gave the order "full speed astern" and to blow three whistles to indicate the vessel's movement full speed astern. *McCulloch* was off the *Governor*'s port bow when the two ships collided, striking the *McCulloch*'s starboard side forward of the pilot house, holing the cutter. All of *McCulloch*'s crew were taken safely aboard *Governor* before the cutter sank to the sea floor 35 minutes later. John Arvid Johansson, *McCulloch*'s acting water tender, was in his bunk and was severely injured during the collision. He died 3 days later in a San Pedro hospital and was buried on June 19th at the nearby Harbor View Cemetery.

Photo: Color Lithograph by Rand McNally, Courtesy Library of Congress

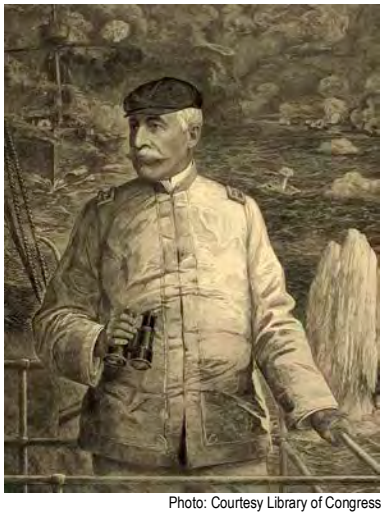

Photo: Courtesy Library of Congress

Photo: Harper's Weekly

Photos: (left) Battle of Manila Bay, May 1, 1898. Manila, Philippines, in the top center, and the Spanish fleet in the upper right. Ships listed descending on the left to bottom: cutter USRC *McCulloch*; gunboats USS *Petrel* and USS *Concord*; protected cruisers USS *Boston*, USS *Raleigh*, USS *Baltimore*, and USS *Olympia* flagship – signaling "Remember the Maine"; (center) Commodore George Dewey on the bridge of the USS *Olympia* during the battle; (right) *McCulloch*'s Chief Engineer Frank B. Randall.

McCulloch – Battle of Manila Bay

On the eve of the Spanish American War, the U.S. Revenue Cutter *McCulloch* was steaming via the Suez Canal and Far East to its first duty station at San Francisco. Upon its arrival at Singapore on April 8, 1898, two weeks before war was declared, *McCulloch* was ordered to report to Commodore George Dewey at the Asiatic station. Dewey's squadron entered Manila Bay on April 30 under the cover of darkness.

Just as *McCulloch* was passing El Fraile Rock, soot in the cutter's stack caught fire and sent up a column of fire. The battery at El Fraile fired at *McCulloch*. The USS *Boston* and *McCulloch* responded, silencing the Spanish guns. Chief Engineer Frank B. Randall died from heat and overexertion while trying to extinguish the smokestack fire, the only American death at the battle. The U.S. squadron destroyed the Spanish warships, killing 381 Spanish seamen. Because of its speed, Dewey ordered *McCulloch* to the nearest cable station located at Hong Kong to dispatch the news of the great naval victory.

USCG Cutter *McCulloch* Expedition 2016

During a joint NOAA – USCG remotely operated vehicle (ROV) training mission in October 2016, the science team confirmed the historic remains of the *McCulloch* off Point Conception, known at the "Cape Horn of the Pacific." Working off the Channel Islands National Marine Sanctuary's R/V *Shearwater*, a VideoRay *Mission Specialist* ROV was deployed to survey and characterize the archaeological remains of this historically significant shipwreck in America's U.S. Coast Guard and U.S. Navy's military history. A team from NOAA, NPS, USCG Dive Locker Alameda and San Diego, with vessel support from USCG District 11 cutters *Halibut* and *Blacktip*, seven successful ROV dives were completed at the shipwreck site. Additional logistical support for the training mission included NOAA's Office of National Sanctuaries (ONMS): Channel Islands National Marine Sanctuary, ONMS Maritime Heritage Program, ONMS West Coast Region Office, USCG District 11, USCG Historian's Office DC and USCG Historian Atlantic Region, VideoRay, and Bathymetric Research.

Photo: Robert V. Schwemmer ONMS NOAA

Underwater Photos: NOAA USCG VideoRay

Photos: (left) NOAA R/V *Shearwater* and USCG Cutter *Halibut* over the *McCulloch* shipwreck site during ROV operations; (center) The helm or steering station was located on the upper-deck of the flying bridge of the USCG Cutter *McCulloch*. The helm is constructed of a nonferrous metal and the wooden handles have succumbed to wood boring organisms; (right) A 6-pounder gun mounted in the sponson located at the starboard bow. The cutter was equipped with four 6-pounder, 3-inch rapid firing guns arranged in sponsons and located in the bow and stern quarters of the ship. The 6-pounder gun was a key diagnostic artifact to identify the shipwreck.